Electrochimica Acta 391 (2021) 138968

Contents lists available at ScienceDirect

Electrochimica Acta

journal homepage: www.elsevier.com/locate/electacta

A peridynamic model for galvanic corrosion and fracture

Jiangming Zhao[a], Siavash Jafarzadeh[a], Mohammad Rahmani[b], Ziguang Chen[c,d], Yong-Rak Kim[b], Florin Bobaru[a,*]

[a] Department of Mechanical and Materials Engineering, University of Nebraska-Lincoln, Lincoln, NE 68588-0526, USA
[b] Zachry Department of Civil and Environmental Engineering, Texas A&M University, College Station, TX 77843-3136, USA
[c] Department of Engineering Mechanics, School of Aerospace Engineering, Huazhong University of Science and Technology, Wuhan 430074, China
[d] Hubei Key Laboratory of Engineering Structural Analysis and Safety Assessment, Wuhan 430074, China

ARTICLE INFO

Article history:
Received 18 June 2021
Revised 15 July 2021
Accepted 19 July 2021
Available online 29 July 2021

Keywords:
Galvanic corrosion
Peridynamics
Electrostatics
Fracture
COMSOL

ABSTRACT

A coupled peridynamic (PD) corrosion-fracture model is introduced, in which the local corrosion rate is determined by solving the corresponding electrostatic problem. By being able to consider variable distributions of corrosion rates along the anodic surface, the model is particularly useful for simulating galvanic corrosion. A novel analytical calibration for parameters in the corrosion model is provided. The corrosion model is verified in terms of the electric potential, current density, and corrosion depth, and validated against experimental results for AE44 (Mg alloy) – mild steel and AE44 – AA6063 (Al alloy) galvanic couples taken from the literature. The PD results are also compared with those from a COMSOL FEM-based model. It is found that an artificial initial "step-down" in geometry at the galvanic joint is required for the COMSOL model in order to provide reasonable results, but it is not needed in the PD model. A coupled galvanic corrosion-fracture problem accounting for the combined electro-chemical attack and strains induced by mechanical loadings is solved.

1. Introduction

Corrosion induced by galvanic coupling can cause deep and rough trenches at the material interface, leading to dangerous situations like other types of localized corrosion, such as pitting corrosion. As stresses rise at these locations, cracks can easily initiate and grow catastrophically. Efficient and accurate predictions of galvanic corrosion problems can help evaluate their effect on engineering structures and provide insights on solutions to prevent it. Due to the simultaneous influence of multiple physical mechanisms involved in galvanic corrosion, computational models are necessary for this purpose. A comparison between different computational models for corrosion can be found in [1]. Major recent advances in galvanic corrosion modeling comes with models based on finite element method (FEM) [2–4] or phase field (PF) method [5,6].

A FEM-based model was developed for galvanic corrosion using the commercial software COMSOL MultiPhysics® (COMSOL hereafter) [2] and validated against the experimental results in [3]. For the galvanic couple between steel and magnesium alloy, although the initial current density and the final corrosion depth obtained by the model have similar patterns to the measured data, the maximum current density and corrosion depth, as well as the transition across the material interface, present nontrivial deviations from the experimental data. A similar model was used in [4] to investigate the effect of mechanical loading on the galvanic corrosion behavior by including stress/strain-dependent electric potential. However, the corrosion pattern obtained by this model, when the mechanical loading is absent, agree even less with those from the experiments shown in [3]. This deviation possibly comes from the linear, instead of piecewise linear, fitting of the polarization curve. The authors of [4] also studied crack initiation in the galvanic couple under uniaxial tension loading by computing the stress intensity factor, approximating the specimen as a side edge notched tensile specimen. As the corrosion front progresses, it departs from such an idealization of the geometry, and these approximations may not be sufficiently accurate. Corrosion depths closer to experimental observations in [3] were obtained in [7,8] by taking into account the effect of corrosion deposition on the corrosion rate.

A PF model for corrosion in galvanic couples was introduced in [5]. However, in the simulation results, the current density distribution does not match well a reference solution given by the FEM-based COMSOL simulation [3]. In addition, the corrosion depth at the junction of the galvanic couple deviates from experimental observation [3] significantly. A different PF model was developed in [6] and was verified against a FEM-based model built in COMSOL,

* Corresponding author.
E-mail address: fbobaru2@unl.edu (F. Bobaru).

https://doi.org/10.1016/j.electacta.2021.138968
0013-4686/

but the polarization was neglected along the corroding interface and no validation tests against experimental data were presented.

One notes that, for these FEM-based /PF models, when corrosion happens at the interface between two joined metal parts, an artificial step-down on the anode side needs to be introduced because of mathematical and numerical inconsistencies [5,6]. As we shall see, in the absence of such a step, an incorrect evolution of the corrosion front is obtained (see discussion in Section 4.2 below). Determining a proper height of this artificial step has not been examined in the published literature. Moreover, with these models based on partial differential equations (PDEs), there is, so far, no attempt to couple galvanic corrosion in a couple with that of crack initiation and propagation. This is partly due to difficulties in being able simulate the complex interactions of these two critical mechanisms: singularities (in classical models), moving-boundary problem, arbitrary geometries, etc.

Recently, the peridynamic (PD) method has been applied to corrosion modeling [9,10]. PD models view corrosion as material damage caused by the dissolution of metal into the electrolyte, coupled with the diffusion of metal ions in the electrolyte [9,10]. A concentration-dependent damage index monitors the evolving corrosion front (phase changes from solid to electrolyte) and the gradual changes in material degradation across the Diffusion-based Corrosion Layer (DCL) [9]. This provides us a better understanding of the factors that lead to the degradation of mechanical properties (strength, ductility, etc.) observed in corroded samples. The PD model has been especially advantageous in simulating stress-corrosion cracking, as shown in the results for pit-to-crack transition obtained in [11].

The existing PD corrosion models, however, use an important simplification: for activation-controlled corrosion, one assumes a constant potential along the corrosion front. The constant potential determines a constant current density from the polarization curve which is measured experimentally. This approach avoids solving for the electric potential distribution along the corrosion front and is acceptable for pitting corrosion cases in which the potential distribution (and therefore the current density) along the pit surface is close to uniform [12]. To cover situations like salt layer formation or passivation at the corrosion front when diffusion-controlled conditions dominate (and the potential distribution varies significantly along the corrosion front), the existing PD models include concentration-based rules that can cause pausing/stopping of metal dissolution as specific locations along the corrosion front [10,13], effectively leading to non-uniform corrosion rates (even if the input corrosion rate is constant). Under activation-controlled conditions, however, these mechanisms are not triggered, and the existing PD corrosion models would not apply to galvanic corrosion problems [14], in which activation-controlled conditions are critical and the electric potential (or the corrosion rate) varies significantly along the corrosion front. Moreover, these variations can also change drastically as the corrosion front evolves. This is the reason why one needs to compute the distribution of the electric potential along the corrosion front in order to predict the evolution of galvanic corrosion.

For galvanic corrosion problems, FEM-based and PF models first evaluate the electric potential by solving the Laplace's/Poisson's equation, with the boundary condition (BC) given by the corresponding metals'/alloys' polarization curves (Tafel's equations). The electric potential determines the current density, which is related to corrosion rate by Faraday's law [2,6,15]. Following a similar procedure, in this paper we introduce a PD electric potential model, and couple it with the existing PD corrosion model [10]. This model is an important extension compared with the previous PD model and will be applicable to a larger class of corrosion problems, including galvanic corrosion. When solving for the electric potential, in order to apply the nonlinear Robin BCs at the arbitrarily-shaped corrosion front and reduce the PD surface effect in the PD electric potential solver, we use a recently introduced autonomous fictitious nodes method (FNM) ([16]).

In addition to introducing the PD electrostatic solver to compute the electric potential, we reformulate the PD corrosion dissolution model in [9,10] based on electrochemistry, and replace the previous numerical calibration stage (which required a trial solution in the pre-processing step) with an analytical one. By eliminating the numerical calibration, the model is significantly more efficient in problems with highly non-uniform current densities along an arbitrary-shape corroding surface, which is often the case in galvanic corrosion problems. The damage-dependent corrosion model used in the original PD corrosion model in [9] is no longer needed. The new model eliminates the required (in order to match the experimental observations) artificial changes to the given geometry of a galvanic couple in models based on PDEs (e.g. COMSOL, phase-field).

We verify the new model for a uniform corrosion 2D case against a classical analytical solution in terms of the electric potential and current density at the beginning of the corrosion process, as well as the evolution of the corrosion depth in time. The model is validated against experimental galvanic corrosion results available in the literature for AE44 (Mg alloy) – mild steel and AE44 – AA6063 (Al alloy) galvanic couples. The results for the initial current density distribution and final corrosion profile are also compared with those from a model built using COMSOL. A coupled corrosion-fracture problem is solved to show the potential of the new PD model in resolving failure caused by the combination of sharp corrosion damage (induced by galvanic corrosion) and mechanical loading.

2. Kinetics of galvanic corrosion

In galvanic corrosion, the metal/alloy with lower corrosion potential is the anode and corrodes first. The ordering of corrosion potential (the galvanic series) for metals/alloys, for a specific environment, is determined from experiments (see pages 171 and 172 in [17]). However, the galvanic series only gives information about the corrosion tendency. The actual corrosion rates of the anode must be determined by separate experiments and the mixed potential theory by overlaying the polarization curves of the constituent individual metals/alloys [2], as schematically shown in Fig. 1.

Electrochemical polarization is the change in electrode potential due to the flow of current (see page 127 in [14]). When the overpotential is small, the corrosion process is activation controlled. In this corrosion type, the current density is governed by Tafel's law:

$$i_a = i_0 \times 10^{\frac{\phi-\phi_0}{\beta}} \tag{1}$$

where i_0 is the uncoupled exchange current density, ϕ is the electrode potential, ϕ_0 is the uncoupled corrosion potential and β is the geometric slope of the linear portion of the semi-logarithmic plot of the polarization curve.

When the overpotential is large, the resulting high anodic dissolution rate saturates the electrolyte near the anode surface, and the corrosion process becomes diffusion controlled. In this case, the current density is determined by concentration changes in reactants or products near an electrode surface. Between these two corrosion types, there exists a transition corrosion type called IR controlled corrosion which is caused by resistance of the electrolyte to the current flow. It happens because there is a finite distance between the reference electrode and the metal surface to be investigated (see pages 130 and 131 in [14]). There are other factors which can affect the corrosion rate, such as the pH field, temperature field, formation of corrosion products, etc. In real corrosion

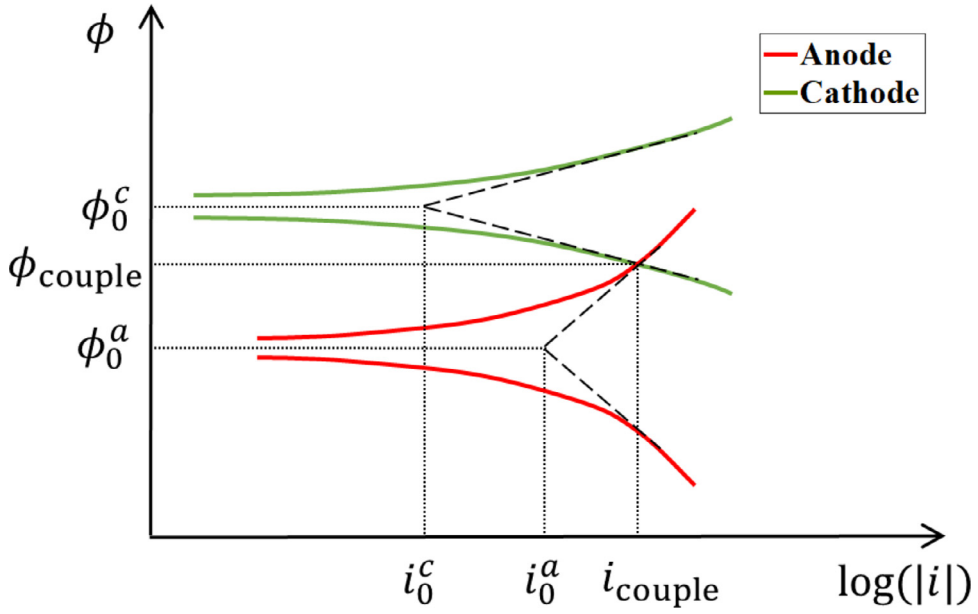

Fig. 1. Schematic polarization curves of anode and cathode in a galvanic couple (see page 177 in [17]). ϕ_0^c and ϕ_0^a are the uncoupled corrosion potential and i_0^c and i_0^a are the uncoupled exchange current density for the cathode and anode, respectively. ϕ_{couple} and i_{couple} are the coupled corrosion potential and current density, respectively.

problems, the corrosion rate is simultaneously influenced by multiple factors and can be determined from the polarization curve measured from corresponding experiments.

For the computational modeling of galvanic corrosion in this work, we focus on the anodic reaction (metal dissolution). The cathodic reaction and the mass transfer in the electrolyte will not be included. Consider an anodic reaction: $M \rightarrow M^{q+} + qe^-$, the current density is formulated by Eq. (1) in which the unknown coefficients are determined by the polarization curve obtained from experiments.

Note that i_a scales linearly with the magnitude of the molar dissolution flux ($|\boldsymbol{J}_{\text{diss}}|$) at the corrosion front via Faraday's law [18]:

$$i_a = qF|\boldsymbol{J}_{\text{diss}}|. \tag{2}$$

where q is the charge number and F is the Faraday's constant. To use Eq. (1) to determine the distribution of current density at the electrode surface, we have to solve for the potential distribution in the electrolyte domain. The electrostatic field satisfies the following Poisson equation [19,20]:

$$\nabla^2\phi = \frac{\rho}{\varepsilon_0} = \frac{\dot{\rho}}{\sigma} \tag{3}$$

where ϕ is the electric potential, ρ is the charge density, ε_0 and σ are the electric permittivity and conductivity of the medium, respectively. For problems in this work, electroneutrality is satisfied in the electrolyte domain, therefore, Poisson's equation reduces to the Laplace's equation:

$$\nabla^2\phi = 0 \tag{4}$$

Rather than using this classical model (Laplace's equation) to approximate the electric potential in the electrolyte for the examples shown in Section 4, we will use the corresponding nonlocal (PD) version of this equation because it will be easier to couple it with the mechanical PD model that we seek to employ for simulating the corrosion and fracture of the sample exposed to galvanic conditions and mechanical loadings. The PD model for the electrostatic solver is given in Section 3.2.1.

3. A coupled PD model for electric potential–driven corrosion and fracture

The PD theory is a nonlocal extension of the classical continuum mechanics [21]. The PD formulation is in the form of integro-differential equations (IDEs) rather than PDEs used in classical local theories. In PD models, discontinuities such as cracks/damages can initiate and propagate naturally and autonomously [22–25]. While the PD method has been primarily used to deal with mechanical behaviors [22,24,26–29], it has also been employed in diffusion-type problems involving cracks and damage, including thermal diffusion [30–33] and mass transport (e.g. corrosion) [1,9,10,13,34–36].

Consider a PD body occupying the domain $\Omega \in \mathbb{R}^k$, $k = 2$ or 3, in which a point $\boldsymbol{x} \in \Omega$ interacts with points $\hat{\boldsymbol{x}} \in \Omega \backslash \boldsymbol{x}$ in a neighborhood $H_{\boldsymbol{x}}$ (called the horizon region of $\boldsymbol{x}$, usually selected to be a disk in 2D, sphere in 3D, centered at $\boldsymbol{x}$). The radius of $H_{\boldsymbol{x}}$ is called the horizon size (or simply, the horizon) and denoted by δ. Objects that carry the pairwise nonlocal interactions between points are called bonds. Fig. 2 schematically shows a PD body with a generic point $\boldsymbol{x}$, its family and its horizon.

In this section we first briefly review the PD mechanical (for fracture) model and then introduce an extended PD corrosion model. Finally, we show how these models are coupled together into a PD corrosion-fracture model. For further discussion on the model the following definitions for solid and liquid domains are useful:

$$\begin{aligned} \Omega_s(t) &= \{\boldsymbol{x} \in \Omega | C(\boldsymbol{x}, t) > C_{\text{sat}}\} \\ \Omega_{\text{diss}}(t) &= \{\boldsymbol{x} \in \Omega | C_{\text{sat}} < C(\boldsymbol{x}, t) < C_{\text{solid}}\} \\ \Omega_l(t) &= \{\boldsymbol{x} \in \Omega | C(\boldsymbol{x}, t) \leq C_{\text{sat}}\} \end{aligned} \tag{5}$$

where C_{solid} refers to the concentration of metal atoms in the intact solid phase, and C_{sat} is the saturation value for dissolved metal atoms in electrolyte. Note that $\Omega_{\text{diss}}(t) \subseteq \Omega_s(t)$.

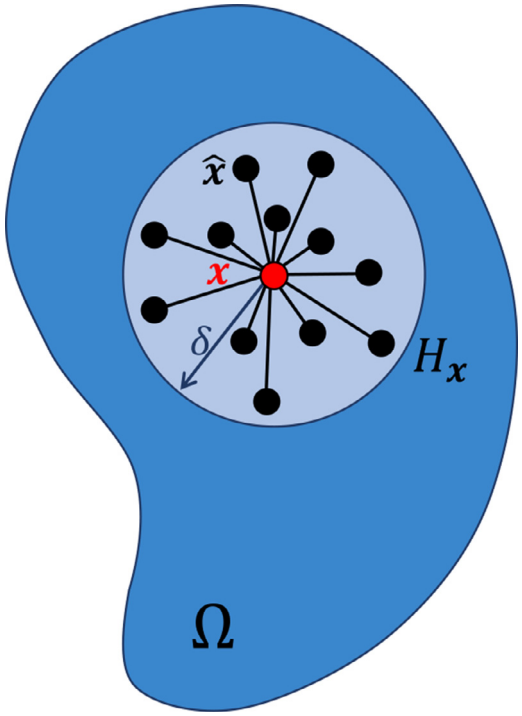

Fig. 2. Nonlocal interaction between point $\boldsymbol{x}$ and an arbitrary point $\hat{\boldsymbol{x}}$ located in its horizon $H_{\boldsymbol{x}}$.

3.1. Bond–based PD mechanical model

The equations of motion for the bond-based PD mechanical model, at each $\boldsymbol{x} \in \Omega_s$, can be written as [22]:

$$\rho(\boldsymbol{x})\ddot{\boldsymbol{u}}(\boldsymbol{x},t) = \int_{H_{\boldsymbol{x}}\cap\Omega_s} \boldsymbol{f}\left(\boldsymbol{u}\left(\hat{\boldsymbol{x}},t\right)-\boldsymbol{u}(\boldsymbol{x},t),\hat{\boldsymbol{x}}-\boldsymbol{x}\right)\mathrm{d}V_{\hat{\boldsymbol{x}}} + \boldsymbol{b}(\boldsymbol{x},t) \tag{6}$$

where t is the time, ρ is the density field, $\boldsymbol{u}$ is the displacement vector field, $\boldsymbol{f}$ is the pairwise force in the PD bond $\boldsymbol{x}-\hat{\boldsymbol{x}}$, and $\boldsymbol{b}$ is the body force field. $dV_{\hat{\boldsymbol{x}}}$ is the volume (area in 2D, length in 1D) associated with $\hat{\boldsymbol{x}}$ that is covered by $H_{\boldsymbol{x}}$. The pairwise force for a prototype micro-elastic brittle material is defined as [22]:

$$\boldsymbol{f} = cs\mu\frac{\boldsymbol{\xi}+\boldsymbol{\eta}}{\|\boldsymbol{\xi}+\boldsymbol{\eta}\|} \tag{7}$$

where $\boldsymbol{\xi} = \hat{\boldsymbol{x}}-\boldsymbol{x}$ is the relative position of $\hat{\boldsymbol{x}}$ and $\boldsymbol{x}$ in the reference configuration, $\boldsymbol{\eta} = \boldsymbol{u}(\hat{\boldsymbol{x}},t)-\boldsymbol{u}(\boldsymbol{x},t)$ is the relative displacement with respect to the reference configuration, c is the micro-modulus function or the elastic stiffness of the bond which can take different forms depending on the required horizon-scale behavior [37], $s = \frac{\|\boldsymbol{\xi}+\boldsymbol{\eta}\|-\|\boldsymbol{\xi}\|}{\|\boldsymbol{\xi}\|}$ is the relative deformation or bond strain. PD bonds break when they reach the critical relative deformation s_0 and the state of a bond is tracked by the bond damage factor μ as [22]:

$$\mu\left(\boldsymbol{x},\hat{\boldsymbol{x}},t\right) = \begin{cases} 1 & \text{if } s\left(x,\hat{\boldsymbol{x}},t'\right) < s_0 \text{ for all } 0 \le t' \le t \\ 0 & \text{otherwise} \end{cases} \tag{8}$$

which means once a bond breaks, it does not carry bond force anymore. With the breakage of bonds, failure starts to accumulate, and cracks begin to initiate and propagate. The damage index d is used to measure the damage level at a point:

$$d(\boldsymbol{x},t) = 1 - \frac{\int_{H_{\boldsymbol{x}}}\mu\left(\hat{\boldsymbol{x}},\boldsymbol{x},t\right)\mathrm{d}V_{\hat{\boldsymbol{x}}}}{\int_{H_{\boldsymbol{x}}}\mathrm{d}V_{\hat{\boldsymbol{x}}}} \tag{9}$$

After spatial discretization, $d(\boldsymbol{x},t)$ is the ratio of the number of broken bonds to that of total bonds connected to point $\boldsymbol{x}$ at time t. When all bonds connected to point $\boldsymbol{x}$ are broken, $d(\boldsymbol{x},t)=1$ and point $\boldsymbol{x}$ becomes a free point. In this work, we consider the constant micro-modulus function [27]. For plane stress conditions, we have $c = \frac{9E}{\pi\delta^3}$ and $s_0 = \sqrt{\frac{4\pi G_0}{9E\delta}}$ (E and G_0 are Young's modulus and energy release rate, respectively), while for plane strain conditions, we have $c = \frac{48E}{5\pi\delta^3}$ and $s_0 = \sqrt{\frac{5\pi G_0}{12E\delta}}$.

For mechanical equilibrium problems with no body forces, but in which damage may evolve in time because of corrosion, Eq. (6) becomes:

$$\int_{H_{\boldsymbol{x}}} \boldsymbol{f}\left(\boldsymbol{u}\left(\hat{\boldsymbol{x}},t\right)-\boldsymbol{u}(\boldsymbol{x},t),\hat{\boldsymbol{x}}-\boldsymbol{x}\right)\mathrm{d}V_{\hat{\boldsymbol{x}}} = 0 \tag{10}$$

where t is the time when equilibrium is tested/enforced after a certain evolution of the corrosion process. Appropriate conditions on the boundaries (volume constraints) have to be assigned to this equation for specific problems. In many cases, it is convenient to enforce these nonlocal BCs to approximate as close as possible the local BCs one would use in a classical model. For each of the examples solved below we describe these conditions in detail.

3.2. PD corrosion model

Corrosion is the result of an electrochemical process. In the presence of electrolytes, metal corrosion can be represented as a dissolution process of the solid material (metal) into the liquid medium (electrolyte). The diffusion of metal ions in the electrolyte can affect the dissolution rate. This process can be effectively described by the original PD corrosion model [9,10], which treats corrosion as a diffusion-type problem in a bi-material system, with specific diffusivities assigned to the solid (an effective diffusivity, not its actual one), liquid and interface phases. Later is was recognized ([10]) that important savings can be achieved by focusing only on the dissolution layer part of the solid (the DCL, Diffusion-based Corrosion Layer [38]) and the electrolyte, as the rest of the solid (with its very small actual diffusivity) does not directly participate in the corrosion process. Specifically, the dissolution flux of metal ions crossing the solid-liquid interface is used in the PD diffusion equation to solve for the metal ion concentration in the bi-material system. The nonlocality in PD models introduces a length scale which facilitates modeling of the dissolution flux, which cannot be defined in local models when jump-discontinuities are present at the interface [10].

The dissolution process causes mechanical damage through a thin layer (several micrometers-thick) at the corroding surface [38–41]. To model mass transport and material damage simultaneously in the PD corrosion model, the material damage definition (d) in Eq. (9) is employed and two sets of bonds are overlaid: transport bonds and mechanical bonds. Transport bonds are responsible for diffusion/dissolution of metal ions/atoms, while mechanical bonds provide the link between strain- and corrosion-induced damage. The corrosion damage process is the progression of material damage/disintegration into the intact material. When the concentration at a solid point drops below the saturated concentration, the point suffers a phase change from solid to electrolyte (its diffusivity is switched to that of the electrolyte), and all of its mechanical bonds are broken (its damage value becomes 1). Material points with a damage value lower than 1 are part of the solid phase: intact ($d=0$, no broken bonds) or partially damaged ($0<d<1$).

Existing PD models for corrosion can capture important changes that happen near the corrosion front (on the solid side) and offer a more complete description of corrosion damage than was possible before [1,9,10,13]. However, in these models, an important simplification is used for activation-controlled corrosion, namely that the overpotential is a constant value (independent of location) along

the corrosion front. This value can be measured from experiments and determines the current density from corresponding polarization curves. This treatment avoids solving for the electric potential distribution along the corrosion front and is acceptable for pitting corrosion cases in which the potential distribution (and therefore the current density) along the pit surface is close to uniform [12]. To cover situations like salt layer formation or passivation at the corrosion front when diffusion-controlled conditions dominate (and the potential distribution varies significantly along the corrosion front), the existing PD models include concentration-based rules that lead to the pausing/stopping of metal dissolution [10,13]. Under activation-controlled conditions, these mechanisms are not triggered, and the existing PD corrosion models would not apply to galvanic corrosion problems [14], in which activation-controlled conditions are critical and the electric potential (or the corrosion rate) varies significantly along the corrosion front. Moreover, these variations also change drastically as the corrosion front evolves. Therefore, to predict galvanic corrosion, it is necessary to compute and update the potential distribution throughout the corrosion process, so that the distribution of corrosion rates along the corrosion front can be updated accordingly.

To achieve this goal, we introduce a PD electrostatic solver to compute the electric potential distribution in the electrolyte domain. In addition to that, we reformulate the PD corrosion dissolution model in [10] based on electrochemistry to substitute the numerical calibration with an analytical one. This change makes the model more reliable for problems with highly non-uniform current densities along arbitrary corroding surface, as in the case of galvanic corrosion. Moreover, we show that the damage-dependent corrosion model which was used in the original PD concentration-dependent damage model is no longer needed.

3.2.1. PD electrostatic model

In galvanic corrosion, one can use the classical model (Laplace's equation) shown in Eq. (4) to find the electric potential. However, because we would like to couple the electric potential solver with the PD corrosion model, it is more convenient (for a seamless integration) to formulate and solve the corresponding PD problem of Laplace's equation in Eq. (4) to find the electric potential needed in the corrosion model. The PD model for finding the electric potential is identical to that for steady state diffusion, with a constant micro-diffusivity:

$$\int_{H_{\boldsymbol{x}}} \frac{\phi(\hat{\boldsymbol{x}}) - \phi(\boldsymbol{x})}{\|\hat{\boldsymbol{x}} - \boldsymbol{x}\|^2} \mathrm{d}V_{\hat{\boldsymbol{x}}} = 0. \tag{11}$$

When using Eq. (11) to solve for the electric potential in the electrolyte, the BCs away from the metal surfaces can be approximated as homogeneous Neumann-type conditions (zero flux across those boundaries). The BC that has to be specified on the metal surfaces, according to the Ohm's law, is:

$$i(\boldsymbol{p}, t) = -\sigma \nabla_{\boldsymbol{n}} \phi(\boldsymbol{p}, t) \tag{12}$$

in which $\boldsymbol{p}$ is a point at the metal surface, σ is the electric conductivity, i is the current density and $\nabla_{\boldsymbol{n}}\phi = \nabla\phi \cdot \boldsymbol{n}$, where $\boldsymbol{n}$ is the outward unit normal. The relation between i and ϕ can be measured experimentally and expressed using Tafel's equation (see Eq. (1)). This makes Eq. (12) a nonlinear Robin type BC [2], written as:

$$i_0 \times 10^{\frac{\phi(\boldsymbol{p},t)-\phi_0}{\beta}} = -\sigma \nabla_{\boldsymbol{n}} \phi(\boldsymbol{p}, t). \tag{13}$$

To enforce the local Robin BC on the metal surfaces in the PD model, we use an autonomous mirror-type fictitious nodes method (FNM) [16], which has been designed to handle boundaries of arbitrary shape. Implementation details are provided in Appendix A. Once the electric potential is obtained, the current density at each point $\boldsymbol{p} \in \partial\Omega$ can be determined by Eq. (13) or the Ohm's law (see Section 3.2.2). For simplicity of implementation, along the zero-flux boundaries, we do not use fictitious nodes, and these conditions are then, approximately, but naturally, represented in the model.

3.2.2. A modified PD corrosion dissolution model

PD corrosion models use a phase-dependent nonlocal diffusion equation on a domain that contains both liquid (electrolyte) and solid (metal) phases. Diffusion of metal ions/atoms in the liquid/solid, and the dissolution of solid into liquid at the solid-liquid interface can all be represented using the PD corrosion model as discussed in [9,10]. In this work, however, we assume activation-controlled conditions, i.e., corrosion rate is not influenced by mass transport in the liquid domain Ω_l (all liquid points are set to always have zero metal-ion concentration). In addition ([10]), mass transport in the solid Ω_s is too slow relative to the interfacial mass transport (dissolution). Therefore, for these conditions we ignore diffusion in Ω_l and Ω_s. Consequently, as shown in Fig. 3 for pitting corrosion, only transport bonds connecting solid and liquid points across the anode surface (pit wall) are involved in the dissolution of solid into liquid. These are called dissolution bonds.

Based on the above assumptions, the PD corrosion dissolution model can be written as:

$$\frac{\partial C(\boldsymbol{x}_d, t)}{\partial t} = \int_{H_{\boldsymbol{x}_d} \cap \Omega_l} J\big(\hat{\boldsymbol{x}}, \boldsymbol{x}_d, t\big) \mathrm{d}V_{\hat{\boldsymbol{x}}} \tag{14}$$

where $C(\boldsymbol{x}_d, t)$ is the concentration at a dissolving point $\boldsymbol{x}_d \in \Omega_{\text{diss}}$ at time t, and the integrand $J(\hat{\boldsymbol{x}}, \boldsymbol{x}_d, t)$ is the mass flow density from $\boldsymbol{x}_d$ to a point $\hat{\boldsymbol{x}} \in H_{\boldsymbol{x}_d} \cap \Omega_l$. In the model presented in [10], J was assumed to depend on the concentration gradient between the ends of a transport bond, $\boldsymbol{x}_d$ and $\hat{\boldsymbol{x}}$:

$$J\big(\hat{\boldsymbol{x}}, \boldsymbol{x}_d, t\big) = \kappa_d \frac{C\big(\hat{\boldsymbol{x}}, t\big) - C(\boldsymbol{x}_d, t)}{\|\hat{\boldsymbol{x}} - \boldsymbol{x}_d\|^2} \tag{15}$$

where κ_d is the constant micro-dissolvability, a parameter that needs to be calibrated such that the dissolution rate in the PD model matches the measured/given activation-controlled corrosion rate. Since there is a linear correlation between κ_d and the current density i [9], i.e., $\kappa_d = \lambda i$, one can find the correlation constant λ by using a trial simulation as follows [10]: a simulation of uniform corrosion under activation-controlled regime is performed with a trial micro-dissolvability κ_d^{trial}; if the resulting current density is denoted by i^{trial}, we have $\lambda = \kappa_d^{\text{trial}}/i^{\text{trial}}$. For cases like galvanic corrosion where i is location-dependent, this would lead to a location-dependent κ_d in Eq. (15), which could be computed from $\lambda i(\boldsymbol{p}(\boldsymbol{x}_d), t)$ (since the electrostatic solver gives the current density value at each point along the metal surface), where $\boldsymbol{p}(\boldsymbol{x}_d)$ is the point in Γ_f (the corrosion front/surface, see Fig. 4) that minimizes the distance to $\boldsymbol{x}_d$. One still would have to find λ, through a calibration procedure. Each set of $\boldsymbol{x}_d$ which share the same $\boldsymbol{p}$ are denoted by $\chi(\boldsymbol{p})$, as shown in Fig. 4 for the case of a smooth boundary.

Since the calibration procedure described above was based on a trial simulation that assumed uniform corrosion for a flat surface, the calibrated value would not be valid on anode surfaces with high curvature (where the radius of curvature is in the order of the horizon size). Such high curvatures are likely to appear in galvanic corrosion in which the corrosion rate can vary significantly along the anode surface, especially near the anode-cathode joint. Moreover, even for flat anode surfaces, this calibration approach would fail to predict the corrosion rate accurately at locations near a corner of the anode (e.g., anode-cathode joint), since dissolving points located near a corner have significantly smaller number of dissolution bonds compared with those which are located elsewhere. This would result in unrealistically slow disso-

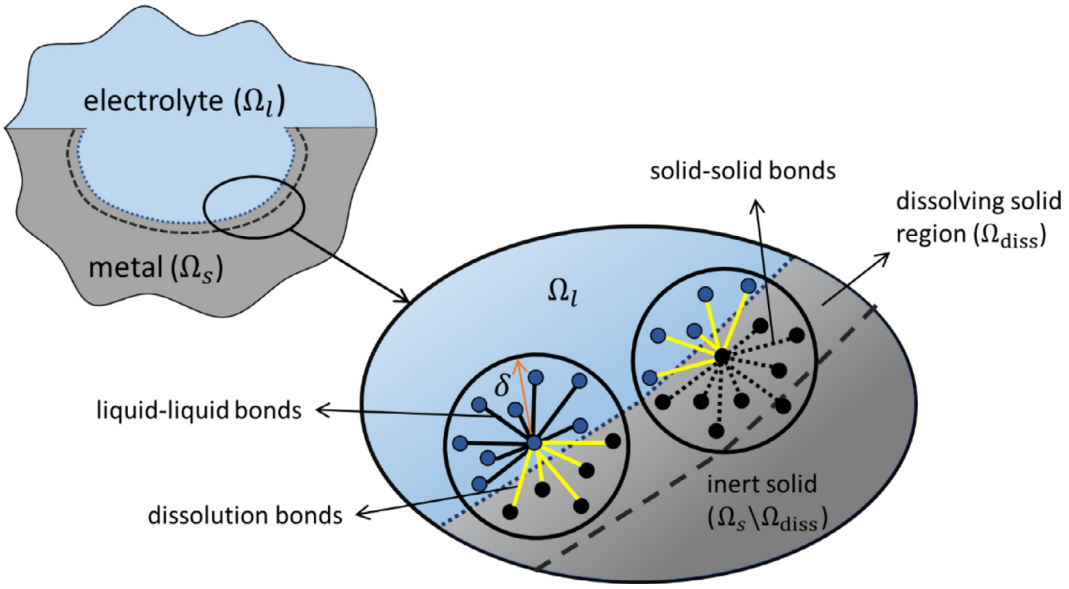

Fig. 3. A schematic of different regions and bonds defined in the PD corrosion model at the corrosion front (redrawn from [10]). The PD horizon size is δ. Solid-solid bonds are considered as inert here, and diffusion in liquid is also ignored (by enforcing zero concentration at all times on liquid nodes).

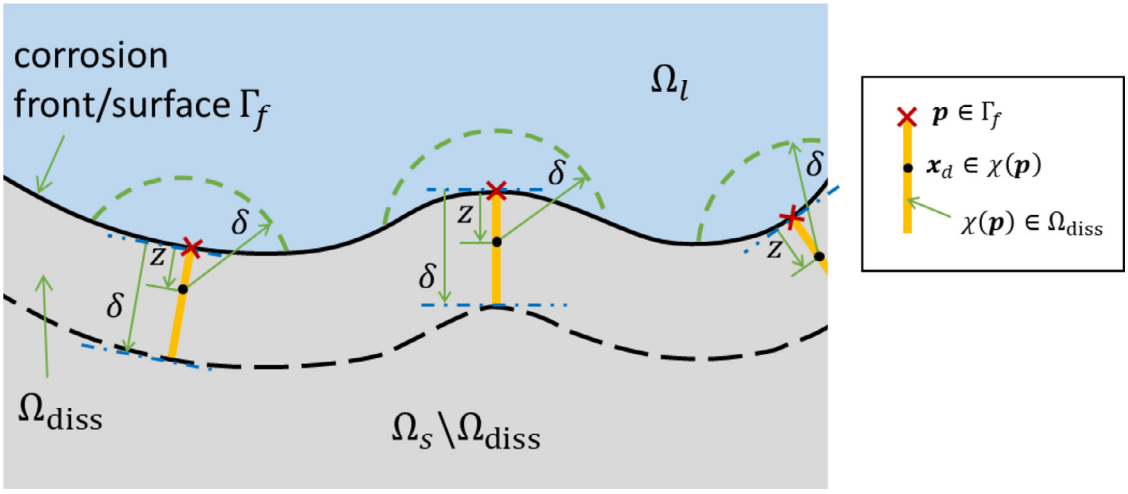

Fig. 4. Examples of dissolving points (that form the set $\chi(\boldsymbol{p})$) which share the current density of point $\boldsymbol{p} \in \Gamma_f$, for an arbitrary, but smooth, boundary.

lution rates at locations which can be critical in the evolution of material damage and failure. For example, the corrosion rate at the anode-cathode joint in galvanic corrosion plays a significant role in material failure since these joints are likely to become stress concentration locations once corrosion starts.

While these issues could be overcome with a series of calibrations performed on a sufficient number of different geometrical configurations of the anode surface, that would lead to a rather complex algorithm/implementation, as well as an increase in the computational cost of the simulation. A preferred option is an analytical, instead of a numerical, calibration for this model parameter. Recall that most PD models are setup using analytical relationships between bond parameters, such as micro-modulus and micro-diffusivity, and material properties, like elastic modulus and diffusivity [22,30].

Furthermore, the dependency of mass flow density in Eq. (15) on concentration distribution becomes less reliable for problems with highly non-uniform current densities along an arbitrary corroding surface, which is the case of galvanic corrosion, for example. From electrochemistry, we know that anodic dissolution is driven by the corrosion reaction (directly related to the current density), which is determined by the potential distribution at the anode surface, and is only indirectly dependent on the concentration distribution near the corrosion front. Therefore, we modify the definition of the PD mass flow density in Eq. (15) to make it directly depend on the current density distribution (determined by the PD electrostatic model, see Section 3.2.1) at the corrosion front, as follows:

$$J\left(\hat{\boldsymbol{x}}, \boldsymbol{x}_d, t\right) = \omega \frac{i(\boldsymbol{p}(\boldsymbol{x}_d), t)}{\|\hat{\boldsymbol{x}} - \boldsymbol{x}_d\|} \tag{16}$$

where ω is a constant that will be calibrated analytically for a certain curvature at $\boldsymbol{p}$ by matching the PD flux $J^{\text{PD}}_{\text{diss}}(\boldsymbol{p}, t)$ (see below) with a given constant dissolution flux $J_{\text{diss}}(\boldsymbol{p}, t)$. Note that here we use a constant ω, but other options are not precluded, for example one could choose $\omega = \omega(\|\hat{\boldsymbol{x}} - \boldsymbol{x}_d\|)$.

Consider a flat surface as shown in Fig. 5, $J^{\text{PD}}_{\text{diss}}(\boldsymbol{p}, t)$ is contributed from all dissolution bonds connected to $\boldsymbol{x}_d \in \chi(\boldsymbol{p})$ and can

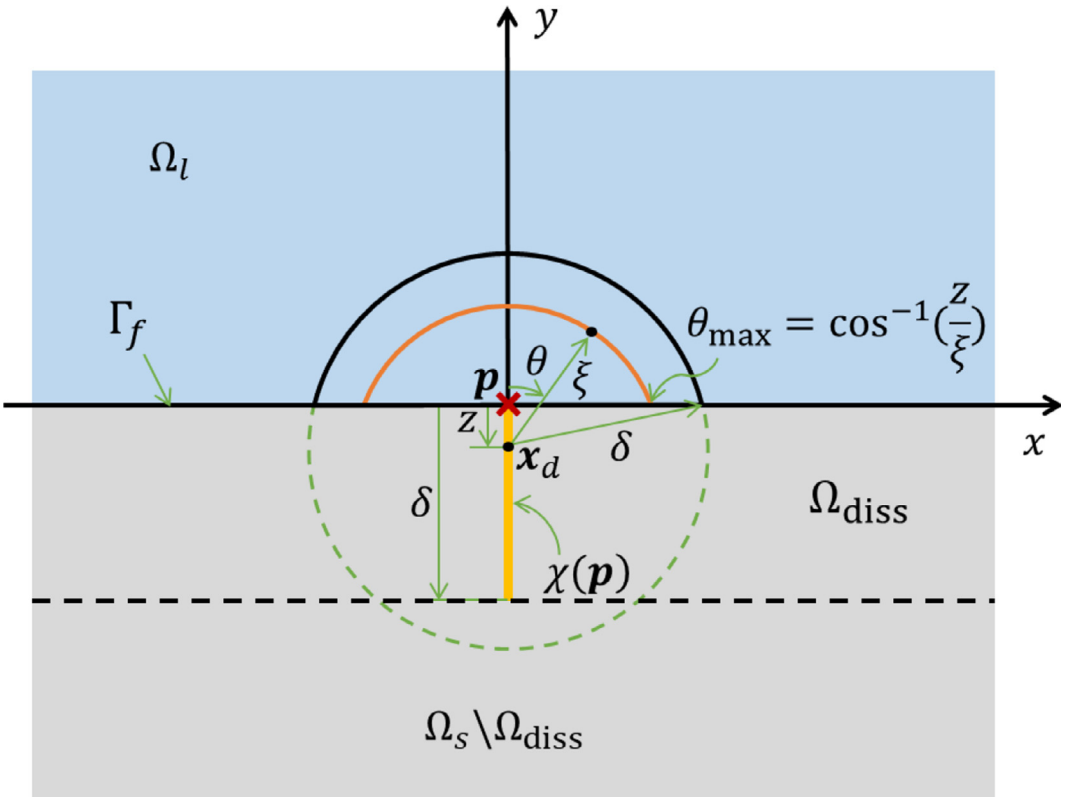

Fig. 5. Computation of the PD flux at a point $\boldsymbol{p}$ at a flat anode surface.

be computed as [25]:

$$J^{\text{PD}}_{\text{diss}}(\boldsymbol{p},t) = \int_0^{\delta}\int_0^{\xi}\int_0^{\cos^{-1}\left(\frac{z}{\xi}\right)} J\left(\hat{\boldsymbol{x}},\boldsymbol{x}_d,t\right)\xi\,\mathrm{d}\theta\,\mathrm{d}\xi\,\mathrm{d}z$$
$$= \int_0^{\delta}\int_0^{\xi}\int_0^{\cos^{-1}\left(\frac{z}{\xi}\right)} \omega\frac{i(\boldsymbol{p},t)}{\xi}\xi\,\mathrm{d}\theta\,\mathrm{d}\xi\,\mathrm{d}z = \omega i(\boldsymbol{p},t)\delta^2 \tag{17}$$

where ξ is the bond length, θ is the angle between the bond and the surface, and z is the distance between $\boldsymbol{x}_d$ and the surface (or $\boldsymbol{p}(\boldsymbol{x}_d)$). Since $J_{\text{diss}}(\boldsymbol{p},t) = i(\boldsymbol{p},t)/qF$ according to Faraday's law, by letting $J^{\text{PD}}_{\text{diss}}(\boldsymbol{p},t) = J_{\text{diss}}(\boldsymbol{p},t)$, we obtain:

$$\omega = \frac{1}{qF\delta^2}. \tag{18}$$

One more step is required to make this model applicable for general corrosion problems, including galvanic corrosion. The PD flux definition in Eq. (17) assumes a flat surface (see Fig. 5). In order to have this analytical calibration process work for the PD transport equation in Eq. (14) independent on the curvature of the anodic surface, we modify the transport equation as described next.

In general, uniform corrosion (same current density i everywhere) on a metal surface of arbitrary shape, as shown in Fig. 4, should evolve perpendicular to the surface and progress with the same speed everywhere. In the PD framework, this means that points $\boldsymbol{x}_d$ with the same distance to the surface (z) should have the same rate of concentration loss, independent of the curvature of the surface at $\boldsymbol{p}(\boldsymbol{x}_d)$ and the number of dissolution bonds connected to $\boldsymbol{x}_d$ (the shape of the horizon region contained in the electrolyte domain, $H_{\boldsymbol{x}_d} \cap \Omega_l$). Therefore, we can write $\frac{\partial C(\boldsymbol{x}_d,t)}{\partial t} = f(z(\boldsymbol{x}_d))$, where $f(z(\boldsymbol{x}_d))$ is the integral of the mass flow density of all dissolution bonds connected to $\boldsymbol{x}_d$, that should not depend on the shape of $H_{\boldsymbol{x}_d} \cap \Omega_l$. Since we calibrated ω for a flat surface, we need to compute $f(z(\boldsymbol{x}_d))$ over a flat surface:

$$f(z(\boldsymbol{x}_d)) = \int_z^{\delta}\int_0^{\cos^{-1}\left(\frac{z}{\xi}\right)} \omega\frac{i(\boldsymbol{p}(\boldsymbol{x}_d),t)}{\xi}\xi\,\mathrm{d}\theta\,\mathrm{d}\xi = 2\omega i(\boldsymbol{p}(\boldsymbol{x}_d),t)$$
$$\times\left\{\delta\cos^{-1}\frac{z}{\delta} - z\ln\left[\frac{\delta}{z} + \tan\left(\cos^{-1}\frac{z}{\delta}\right)\right]\right\}. \tag{19}$$

The modification to the PD model for corrosion dissolution defined by Eqs. (14) and (15) is:

$$\frac{\partial C(\boldsymbol{x}_d,t)}{\partial t} = 2\omega i(\boldsymbol{p}(\boldsymbol{x}_d),t)\left\{\delta\cos^{-1}\frac{z}{\delta} - z\ln\left[\frac{\delta}{z} + \tan\left(\cos^{-1}\frac{z}{\delta}\right)\right]\right\}. \tag{20}$$

Therefore, we replace the integro-differential model in Eqs. (14) and (15) with an ordinary differential model (Eq. (20)) in which $z(\boldsymbol{x}_d)$ for each $\boldsymbol{x}_d \in \Omega_{\text{diss}}$, together with $i(\boldsymbol{p}(\boldsymbol{x}_d),t)$, determines the dissolution flux. Note that computing the distance $z(\boldsymbol{x}_d)$ is, in a sense, computationally equivalent to evaluating the integral in Eq. (14), because it involves, after discretization, searching through the nodes in $H_{\boldsymbol{x}_d} \cap \Omega_l$ for the one closest to $\boldsymbol{x}_d$.

We remark that if we wanted to calibrate ω using a surface different than a flat one, we would have to use that same geometry for computing $f(z(\boldsymbol{x}_d))$. Eq. (20) works naturally for cases where i is highly location-dependent, or when the curvature of the corrosion surface is high (at corners, for example). In Section 4.1, we will use the discrete version of Eq. (20) to estimate the numerical error of resulting current density introduced by the discretization, for a problem with a known (classical) analytical solution.

We now explain how to find the corresponding $\boldsymbol{p}$ and the distance to the surface z, for a given $\boldsymbol{x}_d$. With the meshfree-type

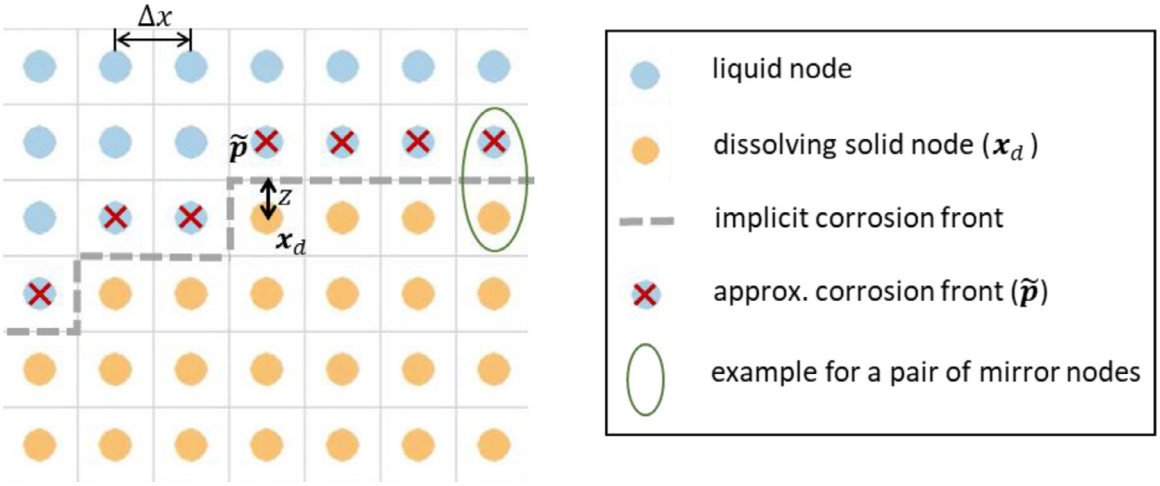

Fig. 6. A schematic of corrosion front after spatial discretization.

(one-point Gaussian quadrature) spatial discretization of the domain (see Fig. 6), the corrosion surface Γ_f is located between the solid nodes and liquid nodes and can be approximated by those liquid nodes $\tilde{\boldsymbol{p}}$ which are closest to solid nodes, as shown in Fig. 6. To determine $\boldsymbol{p}(\boldsymbol{x}_d)$, we search all $\boldsymbol{x} \in H_{\boldsymbol{x}_d} \cap \Omega_l$ for the one closest to $\boldsymbol{x}_d$. If there are multiple such points, we select the one which makes the angle between $\overrightarrow{\boldsymbol{x}_d \tilde{\boldsymbol{p}}}$ and the nonlocal outward unit "normal" at $\boldsymbol{x}_d$, $\boldsymbol{n}(\boldsymbol{x}_d)$, the smallest. The nonlocal outward unit "normal" at $\boldsymbol{x}_d$ (which approximates the classical outward normal on the boundary of a domain) is [16]:

$$\boldsymbol{n}(\boldsymbol{x}_d) = \frac{\int_{H_{\boldsymbol{x}_d} \cap \Omega_l} \left(\hat{\boldsymbol{x}} - \boldsymbol{x}_d\right) d\hat{\boldsymbol{x}}}{\left\| \int_{H_{\boldsymbol{x}_d} \cap \Omega_l} \left(\hat{\boldsymbol{x}} - \boldsymbol{x}_d\right) d\hat{\boldsymbol{x}} \right\|} \tag{21}$$

Since we are not tracking the corrosion front with a moving mesh (we use a fixed and uniform discretization), to improve the approximation of current density distribution along Γ_f, we take $z(\boldsymbol{x}_d) \approx ||\boldsymbol{x}_d - \tilde{\boldsymbol{p}}|| - \frac{\Delta x}{2}$, and used it in Eq. (20).

We compute the current density $i(\tilde{\boldsymbol{p}}, t)$ from Ohm's law:

$$i(\tilde{\boldsymbol{p}}, t) = \sigma \frac{\left|\phi(\tilde{\boldsymbol{p}}, t) - \phi\left(\tilde{\boldsymbol{p}}^R, t\right)\right|}{\| \tilde{\boldsymbol{p}}^R - \tilde{\boldsymbol{p}} \|}. \tag{22}$$

Here, $\tilde{\boldsymbol{p}}^R$ is the reflection/mirror node of $\tilde{\boldsymbol{p}}$ (see Appendix A) through Γ_f and $\phi(\tilde{\boldsymbol{p}}^R, t)$ is the electric potential assigned at $\tilde{\boldsymbol{p}}_m$ to enforce the local BC for the electric potential solver as discussed in Section 3.2.1 and Appendix A. If the polarization curve (or Tafel's equation) is used, we can also compute $i(\tilde{\boldsymbol{p}}, t)$ using Eq. (13) with $\phi(\tilde{\boldsymbol{p}}, t) = \frac{1}{2}[\phi(\tilde{\boldsymbol{p}}, t) + \phi(\tilde{\boldsymbol{p}}^R, t)]$.

3.2.3. Concentration–dependent damage models in PD simulation of corrosion

Modeling of corrosion-induced damage is important in understanding stress-corrosion cracking [42]. In the combined action of mechanical loading and environmental attack, material damage can be caused by strain- or chemically-induced atomic bond rupturing. In the corresponding PD model, we will account for damage accumulation (see Eq. (9)) from both sources: corrosion-induced damage (monitored by $d_c(\boldsymbol{x}, t)$) and mechanical strain-triggered damage (monitored by $d_s(\boldsymbol{x}, t)$). Note that, in the context of corrosion, Eq. (8) is augmented so that the condition for $\mu = 0$ includes corrosion-induced bond breaking.

A concentration-dependent damage (CDD) model was introduced in [9] to establish a relationship between corrosion and the damage of mechanical bonds. Given the intrinsic randomness of the corrosion reaction (partly due to the variations in the microstructure of the material), one can assign a probability $P(\boldsymbol{x}, t)$ of the bonds connected at $\boldsymbol{x} \in \Omega_s$ at time t to break, based on the concentration drop at $\boldsymbol{x}$, for all (intact) mechanical bonds connected to $\boldsymbol{x}$. In order to determine $P(\boldsymbol{x}, t)$, a linear dependency between the corrosion-induced damage $d_c(\boldsymbol{x}, t)$ and the concentration $C(\boldsymbol{x}, t)$ was proposed in [9]:

$$d_c(\boldsymbol{x}, t) = \begin{cases} 1, C(\boldsymbol{x}, t) \le C_{\text{sat}} \\ \frac{C_{\text{solid}} - C(\boldsymbol{x}, t)}{C_{\text{solid}} - C_{\text{sat}}}, C_{\text{sat}} < C(\boldsymbol{x}, t) \le C_{\text{solid}} \end{cases} \tag{23}$$

where C_{solid} refers to the concentration of metal atoms in the intact solid phase, and C_{sat} is the saturation concentration for metal ions in electrolyte. Reaching C_{sat} was assumed as a good approximation for when the solid-to-liquid phase-change takes place. Note that for activation-controlled corrosion, we assume that if a nodal concentration reaches below C_{sat}, that concentration is set to zero. The change in damage (from one time-step to the next, at a point) can then be expressed in terms of the probability $P(\boldsymbol{x}, t)$ as [9]:

$$\Delta d_c(\boldsymbol{x}, t_i) = d_c(\boldsymbol{x}, t_i) - d_c(\boldsymbol{x}, t_{i-1}) = (1 - d_c(\boldsymbol{x}, t_{i-1}))P(\boldsymbol{x}, t_i) \tag{24}$$

Combining Eqs. (23) and (24), one finds an expression for the probability of corrosion damage at $\boldsymbol{x} \in \Omega_s$ and t_i in terms of the concentration drop at that point:

$$\begin{aligned} P(\boldsymbol{x}, t_i) &= \frac{1}{1 - d_c(\boldsymbol{x}, t_{i-1})} \left(\frac{C(\boldsymbol{x}, t_{i-1}) - C(\boldsymbol{x}, t_i)}{C_{\text{solid}} - C_{\text{sat}}} \right) \\ &= \frac{C(\boldsymbol{x}, t_{i-1}) - C(\boldsymbol{x}, t_i)}{C(\boldsymbol{x}, t_{i-1}) - C_{\text{sat}}} \end{aligned} \tag{25}$$

This quantity now allows us to break a corresponding number of mechanical bonds connected to $\boldsymbol{x}$ so that the damage evolves (stochastically) according to Eq. (23). The stochastic procedure for selecting which mechanical bond breaks at a given time $\forall \boldsymbol{x} \in \Omega_s$ is as follows [9]:

(1) Compute/update the concentration field at this time step.
(2) Loop over all $\boldsymbol{x} \in \Omega_s$.
  a Compute the probability of breaking P at $\boldsymbol{x}$; if $P = 0$, then skip this $\boldsymbol{x}$, else continue.
  b Loop over all $\hat{\boldsymbol{x}} \in H_{\boldsymbol{x}} \cap \Omega_s$.
    i If the mechanical bond connecting $\boldsymbol{x}$ and $\hat{\boldsymbol{x}}$ is already broken, then skip this bond, else continue.
    ii Generate a random number $R(\boldsymbol{x}, \hat{x})$ from a uniform distribution in interval $[0, 1]$; if $R(\boldsymbol{x}, \hat{x})$ is smaller than or equal to P, then break the bond (note that each bond

connects two points, thus, once a bond breaks, it is considered broken for both points).

c End loop over all $\hat{\boldsymbol{x}} \in H_{\boldsymbol{x}} \cap \Omega_s$.

(3) End loop over all $\boldsymbol{x} \in \Omega_s$.

Note that Eq. (23) gives the expected corrosion-induced damage value d_c at point $\boldsymbol{x}$, based on the concentration drop at that point only. After performing the bond-breaking procedure for all $\boldsymbol{x} \in \Omega_{\text{diss}}$, the damage index d at each $\boldsymbol{x} \in \Omega_s$ is computed from Eq. (9). However, as we can see in this procedure, a mechanical bond $\boldsymbol{x} - \hat{\boldsymbol{x}}$ can be broken due to either $\boldsymbol{x}$ or $\hat{\boldsymbol{x}}$, which means that the damage index at a point $\boldsymbol{x} \in \Omega_s$, at the end of a time step, can also be affected by bond-breaking events due to concentration drop at $\hat{\boldsymbol{x}} \in H_{\boldsymbol{x}} \cap \Omega_{\text{diss}}$. This means that the damage index computed by Eq. (9) may have a slightly larger values than what is expected from Eq. (23). As a result, there could be material points that reach $d = 1$ (totally detached from other solid points) that still have $C > C_{\text{sat}}$. Physically, this would mean that a small part of the solid (a speck, defined by a node) is now surrounded by electrolyte and would dissolve rather instantaneously. This leads to the conclusion that we can assume this location to, effectively, now be electrolyte phase. This was the reason for the damage-dependent corrosion (DDC) model to be used in [9], where such nodes where switched from a the solid phase to the liquid phase (by changing the micro-diffusivity of transport bonds connected to them). In the absence of DDC, given the "effective" diffusion in solid used in [9] to calibrate the model to a given corrosion rate, one obtains an ever expanding corrosion-affected layer, which is not physically observed (see [38]).

An important update to the CDD + DDC model in [9] has appeared in [10]. There, it was recognized that it was sufficient to monitor changes in the Diffusion-based Corrosion Layer (DCL, a layer of thickness δ at the corrosion surface), and only model transport through PD transport bonds whose end nodes are either solid-liquid or liquid-liquid. The numerical calibration to match a certain corrosion rate for the model in [10] was performed to determine the micro-dissolvability of an dissolution (anode-liquid) bond, as explained above in the paragraph after Eq. (15). While the DDC part of the coupled corrosion-damage model was still used in [10], it had become redundant. Because of the numerical calibration procedure, the model in [10] can work with or without the DDC part. However, the new PD formulation for corrosion dissolution, see Eq. (20), introduced here, does not work with DDC because it uses an analytical calibration, which assumes dissolution happens only through dissolution bonds, and phase-change takes place only when the concentration at a node drops below C_{sat}:

$$\begin{cases} \text{if } C(\boldsymbol{x},\ t) \le C_{\text{sat}} \text{ then } x \in \Omega_l \\ \text{if } C_{\text{sat}} < C(\boldsymbol{x},\ t) \le C_{\text{solid}} \text{ then } x \in \Omega_s \end{cases}. \tag{26}$$

In the context of the new coupled corrosion-damage model, Eqs. (20) and (25), adding the DDC part would artificially speed up the corrosion rate. Therefore, the coupled corrosion-induced damage model we use here is based on Eqs. (20), (25), and (26).

3.3. PD corrosion–fracture model

In previous sections, we reviewed the mechanical fracture model and introduced different ingredients of the modified corrosion model. In this section, we introduce the coupling strategy for these models and discuss their numerical implementation.

The elasticity (with fracture), electrostatics, and mass transfer (with damage and phase-change) models are coupled into a PD model called the PD corrosion-fracture (PD-CF) model and consists of the following set of equations:

Elasticity Eqs. (7) and ((10)):

$$\int_{H_{\boldsymbol{x}}} cs\mu \frac{\boldsymbol{\xi}+\boldsymbol{\eta}}{\boldsymbol{\xi}+\boldsymbol{\eta}} \mathrm{d}V_{\hat{\boldsymbol{x}}} = 0 \ \forall \boldsymbol{x} \in \Omega_s \text{ (displacement)} \tag{27}$$

where $s = \frac{\|\boldsymbol{\xi}+\boldsymbol{\eta}\| - \|\boldsymbol{\xi}\|}{\|\boldsymbol{\xi}\|}$ (bond strain)

Electrostatics Eqs. (11) and ((22)):

$$\int_{H_{\boldsymbol{x}}} \frac{\phi(\hat{\boldsymbol{x}}) - \phi(\boldsymbol{x})}{\|\hat{\boldsymbol{x}} - \boldsymbol{x}\|^2} \mathrm{d}V_{\hat{\boldsymbol{x}}} = 0 \ \forall \boldsymbol{x} \in \Omega_l \text{ (electric potential)}$$

$$i(\widetilde{\boldsymbol{p}}, t) = \sigma \frac{\left|\phi(\widetilde{\boldsymbol{p}}, t) - \phi\left(\widetilde{\boldsymbol{p}}^R, t\right)\right|}{\|\widetilde{\boldsymbol{p}}^R - \widetilde{\boldsymbol{p}}\|} \text{ (current density)} \tag{28}$$

Corrosion Eqs. (20), ((25) and (26)):

$$\frac{\partial C(\boldsymbol{x}, t)}{\partial t} = 2\omega i(\boldsymbol{p}(\boldsymbol{x}), t) \left\{ \delta \cos^{-1}\frac{z}{\delta} - z \ln\left[\frac{\delta}{z} + \tan\left(\cos^{-1}\frac{z}{\delta}\right)\right]\right\} \forall \boldsymbol{x}$$

$$\in \Omega_{\text{diss}} \text{ (mass transport)}$$

$$P(\boldsymbol{x}, t_i) = \frac{C(\boldsymbol{x}, t_{i-1}) - C(\boldsymbol{x}, t_i)}{C(\boldsymbol{x}, t_{i-1}) - C_{\text{sat}}} \forall \boldsymbol{x}$$

$$\in \Omega_s \text{ (bond} - \text{breaking probability)}$$

$$\begin{cases} \text{if } C(\boldsymbol{x},\ t) \le C_{\text{sat}} \text{ then } x \in \Omega_l \\ \text{if } C_{\text{sat}} < C(\boldsymbol{x},\ t) \le C_{\text{solid}} \text{ then } x \in \Omega_s \end{cases} \text{(phase} - \text{change)} \tag{29}$$

Bond damage (corrosion- and strain-induced bond breaking) is defined as:

$$\mu\left(\boldsymbol{x}, \hat{\boldsymbol{x}}, t\right) = \begin{cases} 1 & \text{if } \boldsymbol{x}, \hat{\boldsymbol{x}} \in \Omega_s \text{ and } s\left(\boldsymbol{x}, \hat{\boldsymbol{x}}, t'\right) < s_0 \text{ and} \\ & R\left(\boldsymbol{x}, \hat{\boldsymbol{x}}, t'\right) > P\left(\boldsymbol{x}, t'\right), \forall t' \in [0, t] \\ 0 & \text{otherwise} \end{cases} \tag{30}$$

where R is the random number generated for each bond in the algorithm given in the previous section.

These equations are accompanied by appropriate initial and BCs. The initial concentration distribution for the corrosion and the local BCs to be enforced for electrostatics and elasticity are specified for each of the examples considered here in Sections 4 and 5. In Appendix A, we explain how we enforce local BCs in PD models.

In the PD-CF model, the elasticity model (Eq. (27)) computes the displacements field ($\boldsymbol{u}$) and bond strains (s) in the solid; the electrostatic model (Eq. (28)) computes the electric potential distribution (ϕ) in the electrolyte and current density distribution (i) on electrode surfaces; the corrosion model (Eq. (29)) updates the distribution of metal concentrations (C), computes the corrosion-induced bond-breaking probability (P) and determines the necessary phase changes from the dissolution process; the damage model (Eq. (30)) updates the strain- and corrosion-induced bond-failure in the solid. To visualize damage results, in a post-processing phase, we determine the total nodal damage index value (d) by Eq. (9). Note that in the PD-CF model, $d(\boldsymbol{x},\ t) \approx d_s(\boldsymbol{x},\ t) + (1 - d_s) \times d_c(\boldsymbol{x},\ t)$ in which d_c represents the corrosion-induced damage index and d_s is mechanical strain-triggered damage index.

The implementation of the PD-CF model is shown in Fig. 7. In the main solver, the corrosion solvers are called at each time-step, and the electric potential and displacement fields are updated at the first time-step and any time step if any of the solid nodes becomes liquid in the previous time step. In the electrostatic solver, because the FNM is used to impose BCs, the electric potential needs to be solved iteratively, with the solution in the domain and constraint in the fictitious region updated after each iteration, until two sequential solutions differ by less than a given tolerance. Since this system is linear, we use the Conjugate Gradient (CG) method to solve it. The Euclidean norm is used to measure the difference between two solutions, and the tolerance

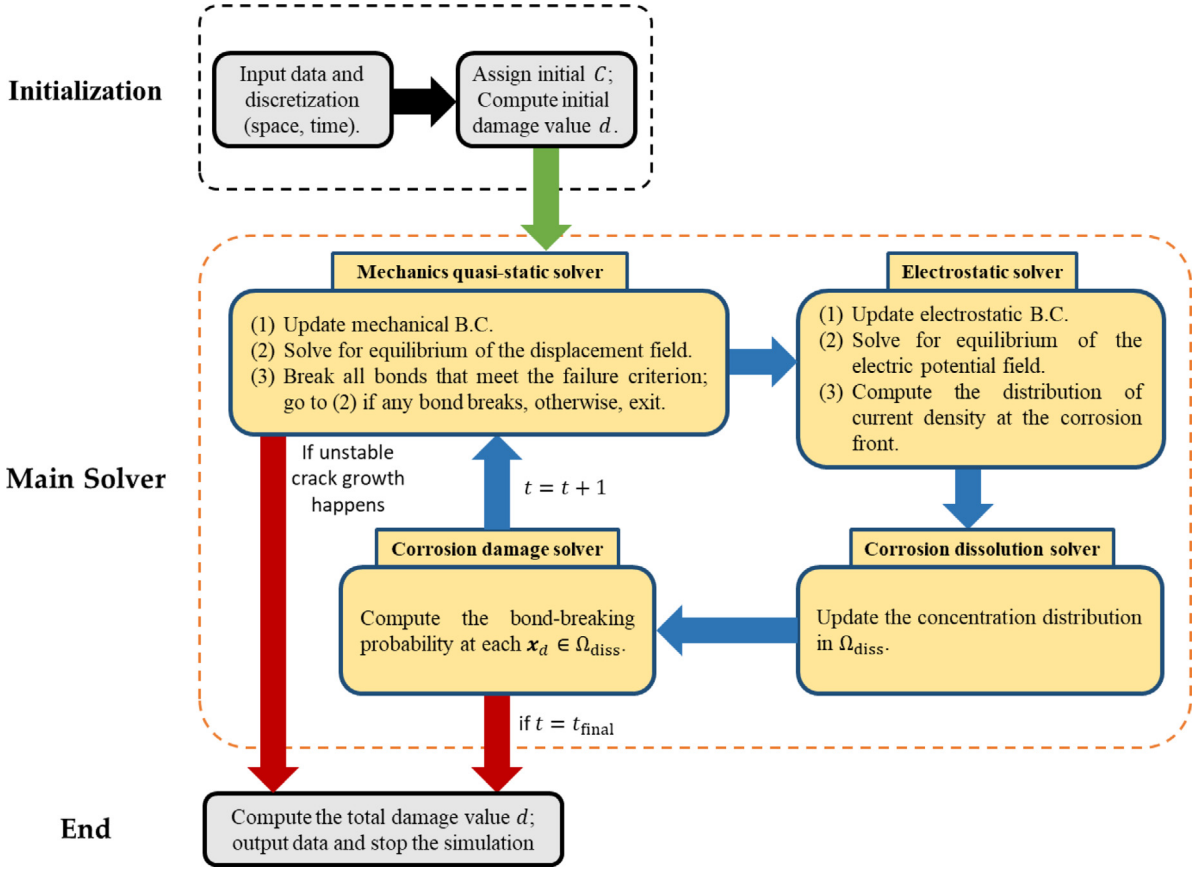

Fig. 7. Workflow of the PD corrosion-fracture (PD-CF) model.

is set to 1e-6. The displacement field is solved by the Nonlinear Conjugate Gradient (NCG) method [43,44] and, ideally, should be updated every time new corrosion damage happens. However, in this work, to save computational time, we update it as frequently as the electric potential field. The influence of this treatment on the stress corrosion cracking behavior is insignificant [11]. If any mechanical bond breaks after we updated the displacement field, the update needs to be repeated until equilibrium is satisfied and no more bonds break in the process. The simulation stops when the final time-step is reached, or when the number of successive updates of displacement field exceed a certain value, e.g., 50, since this would be an indication of unstable crack growth, and a different solver (e.g., explicit) may need to be used.

The corrosion rate may depend on the stress field [36]. While we will show an example solving a coupled corrosion-fracture problem (in which changes in sample geometry induced by the galvanic dissolution process leads to higher tensile stresses/strains and fracture) in Section 5, here we assume the corrosion rate to be independent of the stress field. It is, however, possible to introduce the stress-dependent corrosion rate model into a PD model of corrosion, as has been presented in [36]. The examples shown in Section 4 do not employ the mechanical solver, because no mechanical loadings are involved. The full model is used in the example in Section 5, where we simulate the combined effects of galvanic corrosion and failure induced by corrosion and mechanical loadings.

To discretize the PD IDEs, we use the meshfree method with one-point Gaussian quadrature, in which handling damage and fracture is natural [24]. Uniform grids are used to discretize the domain, both electrolyte and solid regions. Detailed descriptions of the discretization used can be found in [10].

4. Verification and validation of the PD corrosion model

In this section, we first verify the new PD corrosion model against a problem with the corresponding classical analytical solution. Then, validation against experimental data is provided. We only consider activation-controlled corrosion, therefore mass transport between any two points in the electrolyte domain is ignored.

4.1. Verification of the new PD formulation for galvanic corrosion

To verify the new corrosion model for galvanic corrosion, we consider the example shown in Fig. 8. The cathode and anode are in electric contact by a perfect conductor, in the presence of an electrolyte with conductivity σ. The electrode potential of cathode and anode are ϕ_c and ϕ_a, respectively. The whole domain is infinite in the x direction and the electrolyte region has an initial height of h_0.

If both electrodes are nonpolarizable, the classical formulation for the electric potential distribution in the electrolyte domain is:

$$\begin{cases} \nabla^2\phi = 0 \\ \phi(x, y = 0, t) = \phi_c \\ \phi(x, y = h(t), t) = \phi_a \end{cases} \tag{31}$$

where $h(t)$ is the height of the electrolyte domain at time t. The classical solution of Eq. (31) is:

$$\phi(y) = \phi_a - \frac{y}{h(t)}(\phi_a - \phi_c) \tag{32}$$

and the mass flux at the anode surface is:

$$J = \frac{\sigma(\phi_a - \phi_c)}{qFh(t)} \tag{33}$$

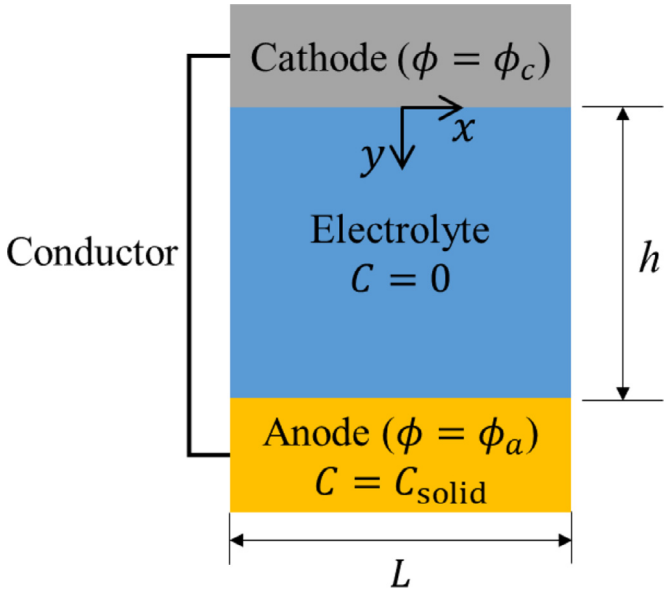

Fig. 8. Sketch of the example used to verify the PD galvanic corrosion model (redrawn from [6]).

Table 1.
Parameter values for the example shown in Fig. 8.

Parameters	Value	Parameters	Value
ϕ_a	0.6 V	F	96,485 C/mol
ϕ_c	0.1 V	h_0	0.1 m
σ	2.5 S/m	L	0.1 m
C_{solid}	143 mol/L	q	2

where q is charge number of a metal ion and F is Faraday's constant. Values for these parameters are provided in Table 1. Note that the width of the domain is set to L in the PD simulation, and periodic BCs are imposed at $x = \pm\frac{L}{2}$, to effectively make the domain infinite in the x direction. To accomplish this, two fictitious regions ($\tilde{A}$ and $\tilde{B}$), with their width equal to the horizon size, are added outside the domain, as shown in Fig. 9. The electric potential in these fictitious regions is mapped from that of the corresponding subdomains (A and B) in the solution domain, so that the left and right boundaries of the solution domain are effectively connected by periodicity.

We first compute the electric potential in the electrolyte domain to verify our PD electrostatic model. We choose $\delta = 4$ mm and $\Delta x = 1$ mm for the simulation. The relative difference (using the Euclidean norm) of the electric potential compared to the classical solution (see Eq. (32)) is 1.67e-6, when the tolerance for convergence is set to 1e-6. The uniform current density at the anode surface computed by Eq. (22) is 12.50183 A/m^2, while the classical solution is 12.5 A/m^2, leading to a relative difference of 1.46e-4. Note that the convergence study on the electric potential is not needed for this problem, because the exact solution has a linear distribution and the FNM enforces the local BCs exactly, i.e., the PD solution matches the analytical classical solution exactly regardless of the grid density. In fact, a finer grid leads to a larger error due to accumulation of round-off numerical errors.

Next, we analyze the numerical error introduced by using the discretized form of Eq. (20) to update the concentration in the corrosion dissolution model. Assuming that at a point on the anode surface the given current density (e.g., obtained from the electric potential) is i_0, the relative difference between i_0 and the resulting current density i_{PD}^m generated by using the discrete form of Eq. (20) can be written as:

Table 2.
Numerical errors (for different values of m) for the resulting current density when the discrete version of Eq. (20) is used to update the concentration in the corrosion dissolution model.

m-value	$\lvert\frac{i_{\text{PD}}^m - i_0}{i_0}\rvert$
2	7.15e-2
4	2.18e-2
8	6.4e-3
16	1.8e-3
32	5.2e-4

$$\left|\frac{i_{\text{PD}}^m - i_0}{i_0}\right| = \left|1 - \frac{2}{m^2}\sum_{k=1}^{m}\left\{m\cos^{-1}\frac{z_k}{m} - z_k \ln\left[\frac{m}{z_k} + \tan\left(\cos^{-1}\frac{z_k}{m}\right)\right]\right\}\right| \tag{34}$$

where m is the ratio of horizon size and grid size ($\delta/\Delta x$), and $z_k = k - 1/2$. This relative error only depends on the value of m and should drop as m increases (or as $1/m$ decreases). The error for different m-values is given in Table 2; as expected, larger m-value leads to smaller error (with a convergence rate close to quadratic). However, as we increase the m-value (with δ fixed), the scaling of the total computational cost also increases significantly, since with this type of numerical solution, the scaling is $O(N^2)$, where N is the total number of nodes used in the discretization [45]. Note also that a larger m-value does not necessarily improve the accuracy because of concurrent increase in round-off error. It is possible to choose different m-values for each model in the coupled PD-CF model to balance cost and accuracy. When a large m-value is needed to capture some fine details, the fast convolution-based PD method recently introduced, may be used as an alternative approach, since it has been shown to lead to significant computational efficiencies [45,46]. Here, considering that the relative error in i_{PD} is acceptable when $m = 4$, we use this value. Note that since we calibrated the PD models, for any horizon size, to match a given current density (see Eq. (18)), these numerical errors are independent of the horizon size.

To verify the coupling of the electrostatic model and the corrosion dissolution model, we test the corrosion evolution for the problem in Fig. 8 by checking the corrosion depth $z_h = (h - h_0)$ as a function of time t. The solution for the corrosion depth in the classical model is [6]:

$$z_h = \sqrt{\frac{2\sigma t(\phi_a - \phi_c)}{qFc_{\text{solid}}} + h_0^2} - h_0 \tag{35}$$

The evolution of corrosion depth obtained by the PD corrosion model (using effective corrosion depth, see Appendix B) agrees with the classical solution, as shown in Fig. 10. The relative difference of the final depth between them is 2.07%, which is close to the numerical error in the effective current density for $m = 4$ shown in Table 2. Note that the relative difference in electric potential between the PD and classical solutions, and the approximation of the current density by Eq. (22), also contribute to the relative difference in corrosion depth between the PD and classical models.

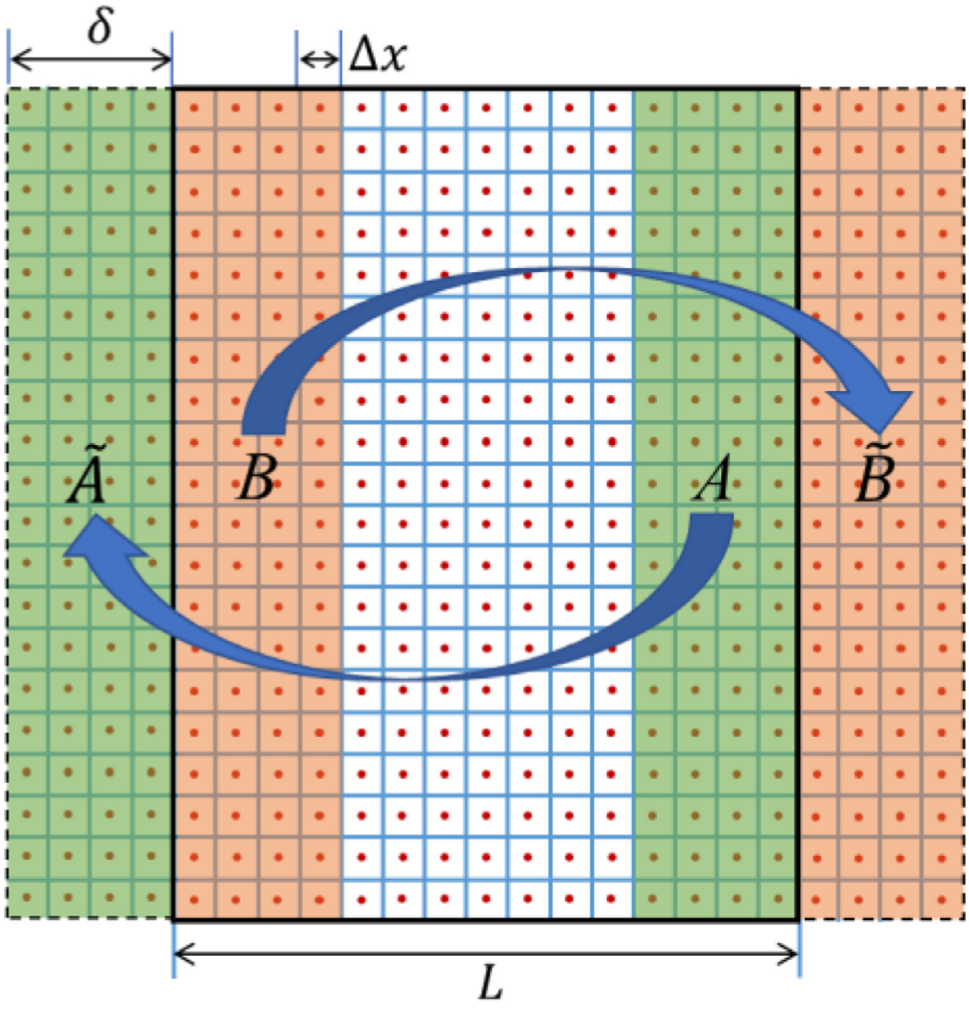

Fig. 9. Schematic of the implementation of periodic BCs in PD simulations.

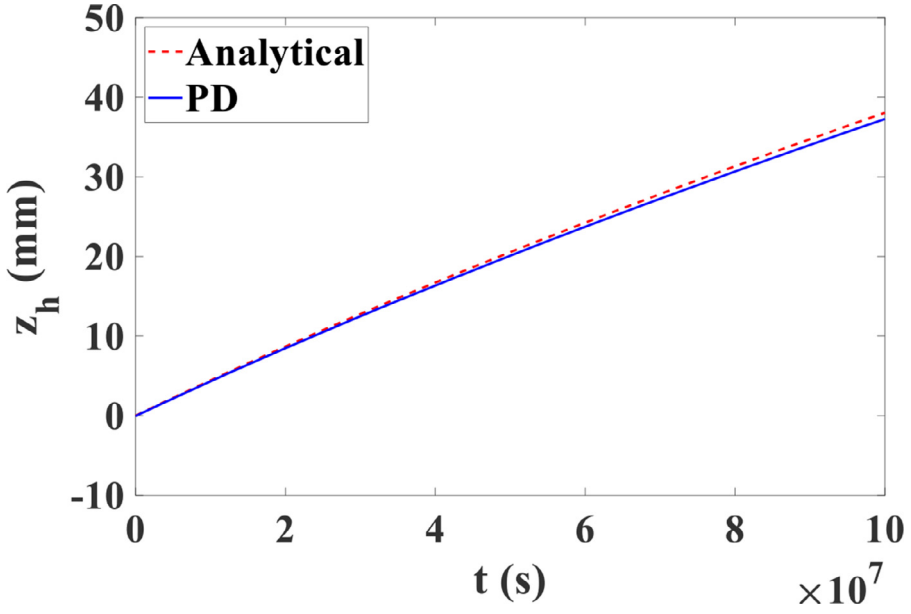

Fig. 10. Comparison of the corrosion depth vs. time between PD solution and classical solution (Eq. (35)) for the problem shown in Fig. 8. Computing the effective corrosion depth in PD corrosion model is described in Appendix B

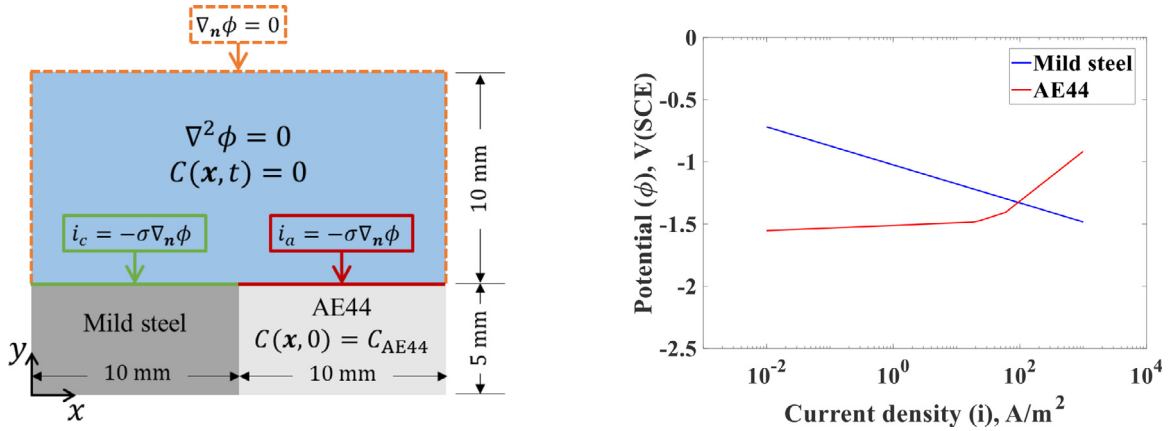

Fig. 11. (a) Geometry and BCs for the galvanic corrosion problem (adapted from [2]); (b) piecewise linear interpolation of the experimentally obtained polarization curves for mild steel and AE44 in [2] (details are given in Table 3).

Table 3.
Data used in the piecewise linear interpolation of the polarization curves from [2] (to be used in the Tafel's equation).

	Alloy	ϕ (V, SCE)	i_0 (A/m^2)	β (V)	ϕ_0 (V, SCE)
Anode	AE44	$(-\infty, -1.48)$	0.014	0.021	−1.55
		$[-1.48, -1.41]$	21.145	0.166	−1.48
		$(-1.41, \infty)$	58.107	0.400	−1.41
Cathode	Mild steel		0.00125	−0.153	−0.58

Table 4.
Material properties for the galvanic problem shown in Fig. 11 (a).

Parameters	σ	C^{AE44}_{solid}	q
Value	2.5 S/m	67860 mol/m^3	2

4.2. Validation against experimental results from the literature

The previous example verified the PD electrostatic model and the modified corrosion dissolution model. In this subsection, we validate the model against a galvanic corrosion experiment which appeared in [3]. We compare the PD results with experimental observations, as well as with results obtained by a FEM-based model built in COMSOL (see Appendix C) for the classical formulation of the problem. The model in COMSOL uses the Arbitrary Lagrangian-Eulerian method to track the corrosion front as a moving boundary [2].

The setup of the problem is shown in Fig. 11 (a). The classical formulation for the electric potential distribution in the electrolyte domain is:

$$\begin{cases} \nabla^2\phi = 0 \\ \nabla_n\phi(x = 0,\ 10 < y < 20, t) = 0 \\ \nabla_n\phi(x = 20,\ 10 < y < 20, t) = 0 \\ \nabla_n\phi(0 < x < 20,\ y = 15, t) = 0 \\ \nabla_n\phi(0 < x < 10,\ y = 5, t) = -i_c/\sigma \\ \nabla_n\phi(10 < x < 20,\ y = 5, t) = -i_a/\sigma \end{cases} \tag{36}$$

in which $\nabla_n\phi = \nabla\phi \cdot \boldsymbol{n}$, i_a and i_c are defined by the Tafel's equation (see Eq. (13)) which can be determined by fitting the polarization curves of corresponding galvanic couples. The polarization curves we use for the AE44 – mild steel couple are shown in Fig. 11 (b) which are (piecewise) linear interpolations of the experimentally obtained curves in [2]. The coefficients in the Tafel's equation are given in Table 3. Note that the sign of cathodic and anodic current densities is negative and positive, respectively. Other material properties for this problem are provided in Table 4. These parameters are used in both PD and COMSOL simulations.

The comparison between COMSOL results and PD results (with $\delta = 0.4$ mm) in terms of the initial potential distribution is shown in Fig. 12. The COMSOL result is selected after a convergence study with respect to the mesh size (see Appendix C for details on the COMSOL model) and then, before plotting, post-processed by the Kriging interpolation (necessary because of the adaptive mesh used in COMSOL) and plotting that at the nodes of the uniform grid used in the PD model. The agreement between the two solutions is very good.

For a quantitative comparison, we plot the initial current density distribution along the electrode surface in Fig. 13. From the zoom-in images, we can see that the PD solution, as the horizon size decreases (m-value is fixed to be 4), approaches the result found by COMSOL. In the experimental results, there is a smooth transition of current density at the galvanic joint, and its minimum value is around -50 A/m^2, while the PD and COMSOL results show much smaller values (around -120 A/m^2), and a sudden jump at the galvanic joint. We notice that, in the experiment (see [2]), the spatial resolution of the current density variation at the joint is highly dependent on the scan rate, or the data acquisition time at each measurement point, but the author did not perform a convergence study on the scan rate. A slower scan rate may lead to sharper transition at the joint. Another possible factor is that, in the real physical system, there exists a transition zone between different materials, while in our models, we assumed a sudden material change at the joint. Note that the difference between the PD and COMSOL results near the interface is due to the finer discretization used by COMSOL near the interface (automatic adaptive refinement).

The experimental profile and that obtained by the PD model for the AE44 – mild steel galvanic couple after 3 days of corrosion are shown in Fig. 14 (a) and (b), respectively. Although the magnitude of corrosion depth obtained by PD simulation is slightly smaller than that from the experiment, their patterns agree very well.

The comparison for the final corrosion depth between experimental measurements, COMSOL and PD results, is shown in Fig. 15. In Appendix B we explain how we computed the effective corrosion depth in the PD corrosion model. The corrosion profile obtained by the COMSOL model differs considerably from the experimental one or the one found by the PD corrosion model. Notice, however, that the results presented in Refs. [5,6,47] show patterns similar to experimental measurements. That is because an artificial step in the geometry of the galvanic joint was used in producing those results. While this artificial step is mentioned in Ref. [31], it was not mentioned in [32] but its insertion is obvious from the plots shown there. To obtain COMSOL results closer to those measured in experiments, we therefore modify the geometry and

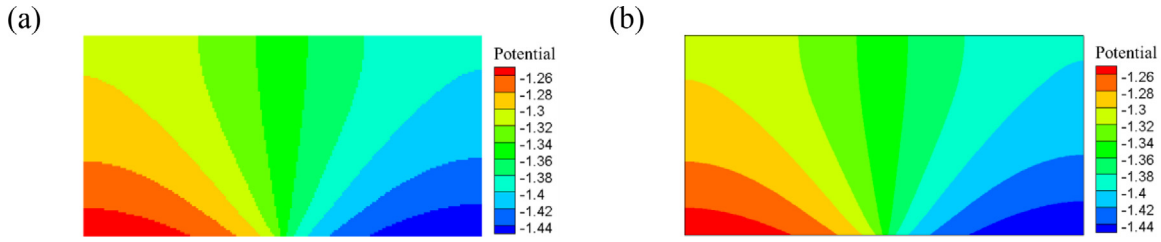

Fig. 12. Electric potential distribution for AE44 – mild steel galvanic couple obtained by (a) PD; (b) COMSOL.

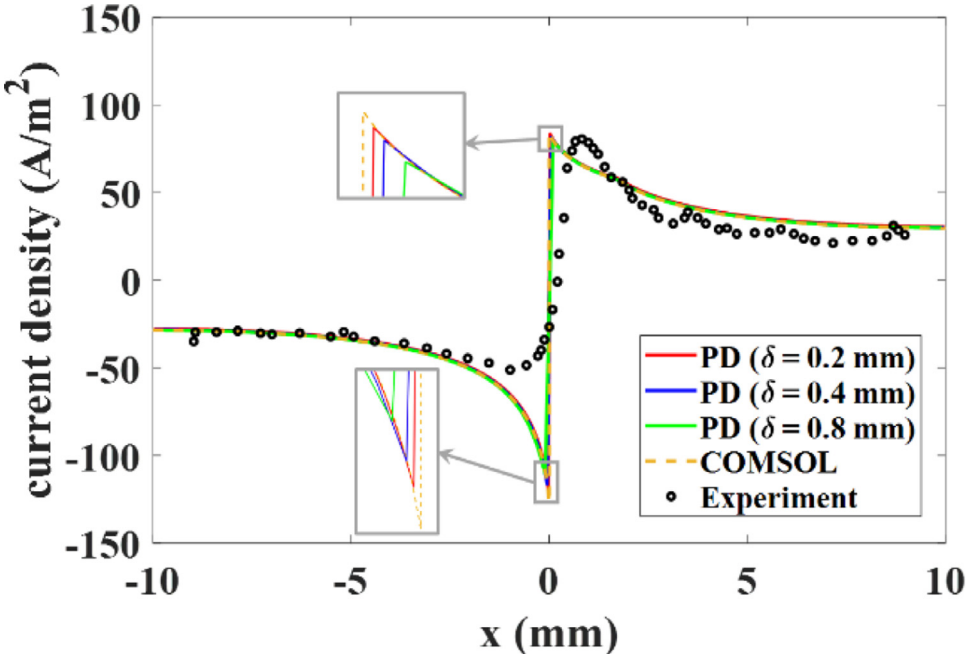

Fig. 13. Initial current density along the electrode surface for AE44 – mild steel couple: convergence study for PD solutions; COMSOL (our work), and experimental results from [3].

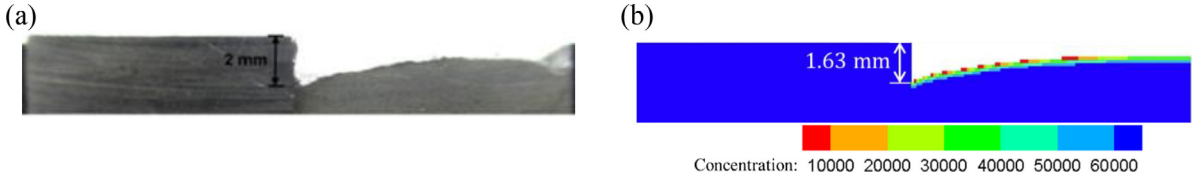

Fig. 14. Corrosion profiles for the AE44 – mild steel galvanic couple obtained from (a) experiments [3]; (b) PD corrosion model ($\delta = 0.4$ mm).

insert the small step at the galvanic joint before the start of the COMSOL simulation. This extra treatment, which reduces the generality of the COMSOL model, is necessary because of difficulties with assigning proper BCs in the classical model at the interface, and it allows the corrosion front to start moving in a way similar to what is observed experimentally (see Appendix C). The size of the artificial step determines the smallest mesh size used, and, as its size goes to zero, the maximum corrosion depth obtained appears to converge, as results shown in Appendix C indicate. Note also that in [2,4], the authors did not specify whether or not they inserted this artificial step into their COMSOL model. However, the corrosion depth profiles for the AE44 – mild steel galvanic couple obtained there show a pattern close to our COMSOL results that use the artificial step, and it is, therefore, reasonable to assume that they made use of the step there as well.

As shown in Fig. 15, both PD and the modified-geometry COMSOL models generate slightly smaller maximum corrosion depths than measured in experiments. Some possible explanations are: (1) the geometry of the electrolyte domain used in simulations is different from the real conditions (our electrolyte "bath" has "walls" at the ends of the sample, while the electrochemical cell used in experiments is likely larger than the sample; also, our model is a 2D approximation of an actual 3D experiment); (2) other corrosion mechanisms, not included here (e.g. crevice or micro-galvanic corrosion, stress-dependent corrosion rate), may accelerate the corrosion at the interface between the anode and the cathode, as well as at the edge of the anode; (3) the deposition of corrosion products on the corrosion surface (not considered here), can affect the dissolution of metal atoms into the electrolyte and the electric potential around the surface and thus impact the evolution of corrosion [7,8]. Note that the specific shape at the bottom of the trench carved by the galvanic corrosion process is very important when mechanical loadings are involved because it affects the stress profile in that critical region, from which cracks can initiate and propagate (see next section). Microscale experimentation that can quantify, in detail, the shape of the bottom of the trench as galvanic corrosion attack progresses, could be used for further validation of the PD models presented here.

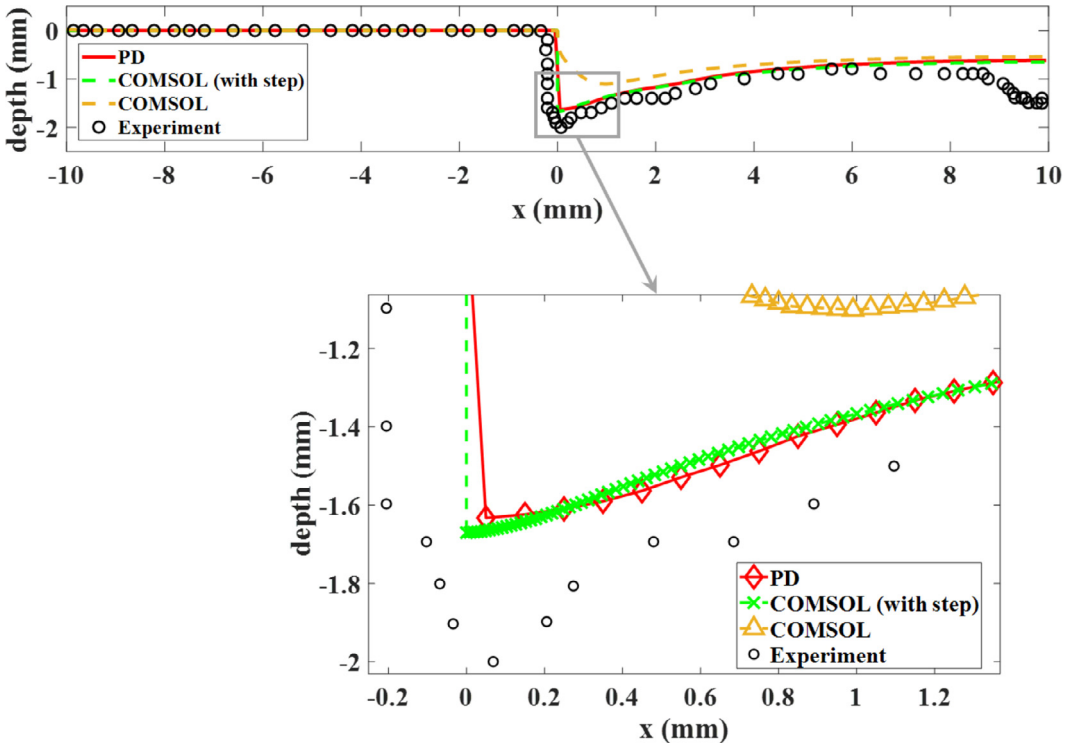

Fig. 15. Corrosion depths obtained from the PD corrosion model ($\delta = 0.4$ mm), COMSOL with and without the artificial step (our work), and experiments from [3] for AE44 – mild steel galvanic couple. See Appendix B for how we computed the corrosion depth in the PD corrosion model.

The COMSOL curve obtained with the artificial step (see Fig. 15), appears to be slightly steeper and deeper at the galvanic interface than the PD curves. This is because: (1) the adaptive mesh refinement technique the COMSOL model employs generates a much finer mesh near the interface than the uniform grid used in PD models, leading to a slightly larger current density at the interface than that obtained by the PD corrosion model (see Fig. 13); and (2), the discretized PD corrosion dissolution model effectively induces a slightly slower corrosion rate, as demonstrated in Section 4.1, that could be mitigated by using a larger m-value (not pursued here due to increasing computational cost).

Note that our galvanic corrosion model is general and work for any kind of galvanic joints, as long as the corrosion processes are well described by the mechanisms included in the model. An additional validation for the AE44 – AA6063 galvanic couple is provided in Appendix D.

The DCL formed below the corrosion front can degrade material's performance, and can play a significant role in material failure when mechanical loadings are applied to the galvanic couple [48]. In the next section, we investigate the coupling of galvanic corrosion and fracture, when both corrosion attack and mechanical loadings are present. Such a multi-physical problem can be easily treated with PD models but is difficult to simulate using classical models.

5. Application of the PD–CF model to galvanic corrosion–induced fracture

In this section, we investigate the coupling effect between galvanic corrosion and mechanical loading on material failure. Galvanic corrosion usually generates localized and deep trenches at a material interface. As stresses rise/concentrate at these locations, cracks can easily initiate and grow catastrophically. To date, no model has attempted to predict the coupling of these two critical mechanisms involved in material degradation and failure. Such a multi-physical problem can be easily treated using PD models.

We consider the 2D thin plate galvanic couple (mild steel and AE44, see Fig. 11 (a)) under plane stress conditions and subject to the mechanical loadings and environmental conditions shown in Fig. 16. As galvanic corrosion progresses at the interface, bending creates a region a higher tensile stresses at the corrosion trench, and a crack may initiate and propagate, if conditions meet the brittle fracture criterion discussed in Section 3.1. Note that the loading conditions and geometry have significant effects on the stress concentration at the joint of the galvanic couple. In addition, once a crack initiates in the region damaged by galvanic corrosion, its stress intensity factor also depends on the loading conditions and geometry [49]. In actual 3D structures, conditions along the crack front vary from plane stress near its edges to plane strain in its central part [49]. The thin plate couple we chose here is only for demonstrating our models' capabilities to handle the coupled effect of galvanic corrosion and fracture induced by it. A full 3D example will be pursued once experimental data for this coupled problem become available.

The local mechanical BCs to be enforced are:

$$\begin{cases} u_y(0 < x < \delta,\ y = 5,\ t) = u_0 \\ u_y\left(-\frac{\delta}{2} < x < \frac{\delta}{2},\ y = 0,\ t\right) = 0 \\ u_x(x = 20,\ 0 < y < 5,\ t) = 0 \\ u_y(x = 20,\ 0 < y < 5,\ t) = 0 \end{cases} \tag{37}$$

In the corresponding PD mechanical model, the displacement on the right side is fixed in all directions through a thickness equal to the horizon size δ. At the left top of the cathode domain, a $\delta \times \delta$ square region is displaced at the start of the simulation by a fixed amount ($u_0 = 50\ \mu$m) and is kept constant in time, while another square region (of same dimension) at the central bottom location of the couple is fixed in the vertical direction. In this example, we choose $\delta = 4$ mm and $\Delta x = 1$ mm.

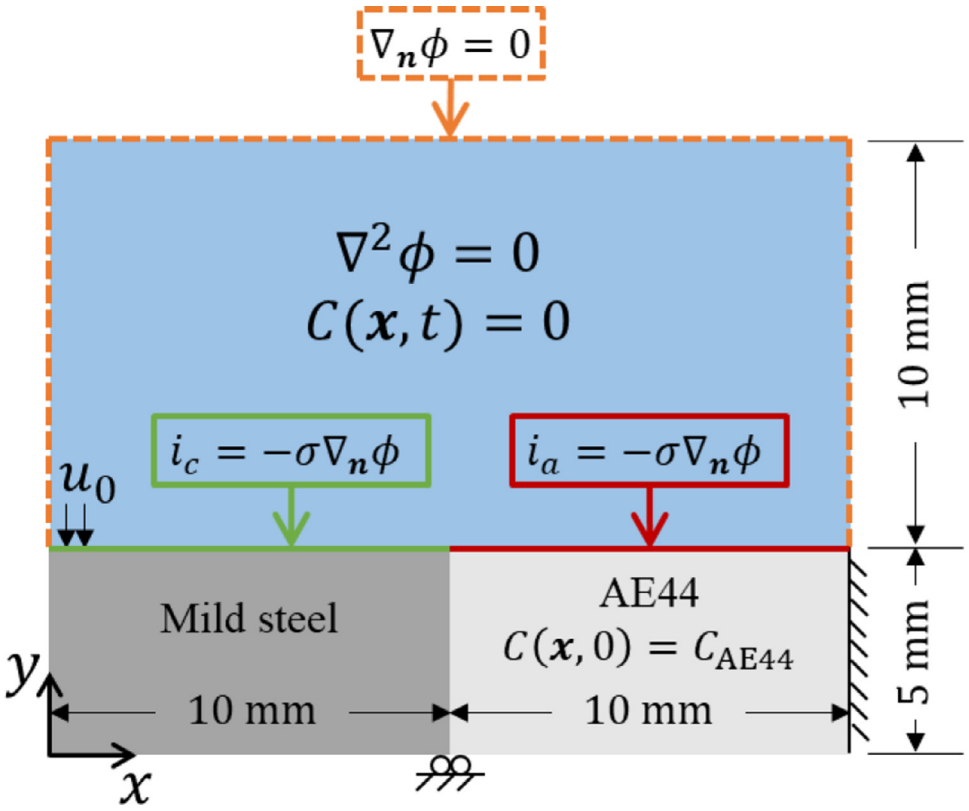

Fig. 16. Geometry and BCs for the galvanic couple under combined mechanical loading and galvanic corrosion attack.

Table 5.
Mechanical properties for materials in the galvanic couple (Fig. 16).

Parameters	Steel	AE44	Interface
Young's modulus (GPa)	205 [51]	45 [52]	125
Fracture energy (kJ/m^2)	65 [53]	1.5 [54]	0.1

Since we did not find experimental data for this type of problem to compare our PD results with, we simply assume a certain fracture toughness (100 J/m^2) for the interface between the metals, to allow a crack to propagate at some point (not too early, not too late) during the formation of the galvanic corrosion trench in our particular example. Material properties for the alloys and the interface are given in Table 5. The Young's modulus for the interface is assumed to be the average of the two alloys [50], i.e., 125 GPa.

As mentioned previously, the DCL reduces the material properties at the corrosion front. According to experimental measurements (performed on a number of material systems, such as Mg and Al alloys), the DCL can be several micrometers thick and is seamlessly attached to the bulk with gradual change of properties [38–40]. Under external loadings, microcracks can accumulate in the DCL in a brittle fashion and grow into the bulk, leading to significant loss of overall ductility in the structure.

Contours of the damage index obtained by the PD simulation for the problem setup seen in Fig. 16 are given in Fig. 17. A simulation movie is also included in Supplementary Materials. The system does not crack under the applied bending loads before corrosion starts, as shown in Fig. 17 (a). As galvanic corrosion progresses, the geometry changes gradually, creating higher and higher tensile stresses at the bottom of the trench. A few PD bonds start to break because of reaching their critical strain (see Section 3.1), but once they do, strains nearby relax and any potential crack growth arrests, and the next call to the corrosion solver is made. After about 41.6 hrs. of corrosion time, as shown in Fig. 17 (c), a crack suddenly initiates and propagates along the interface. The crack arrests at some point before reaching the bottom of the interface, because of the displacement-controlled BCs. Note that here we only considered a brittle fracture model. Plastic deformations can also strongly influence crack growth but were not considered in this work.

While galvanic corrosion influences the state of stress in our model (by changing the geometry of the sample as the corrosion trench increases), we did not consider here stress-dependent corrosion rate, the possible direct effect tensile stresses could have on the corrosion itself. A PD model that uses a stress-dependent corrosion rate has been introduced and validated in [11,36]. We do not consider it here for simplicity, but once experimental data on the coupled corrosion-fracture problems become available, such a model can easily be tested. For the same reason, we do not account for the conditions that are specific to crevice corrosion, which has been recently investigated with a PD model in [55]. The example chosen here is demonstrate that possible coupling of degradation due to galvanic corrosion and that due to critical strains that take place in the trench created by the galvanic corrosion process.

Note also that temperature can have a significant influence on the corrosion rate, as well as on the mechanical properties (elasticity, plasticity, fracture). Our model can incorporate such dependencies easily and examples of such effects in thermomechanical fracture have been shown using PD formulations in, e.g. [44]. Such dependencies are, however, beyond the scope of the present work.

To solve this coupled problem using COMSOL or other PDE-based classical models, one needs to consider a model for crack growth. One option is to use cohesive elements with their corresponding damage models defined throughout the domain of interest. Beside the complexity of coupling these physical mechanisms, introducing cohesive elements can significantly increase the com-

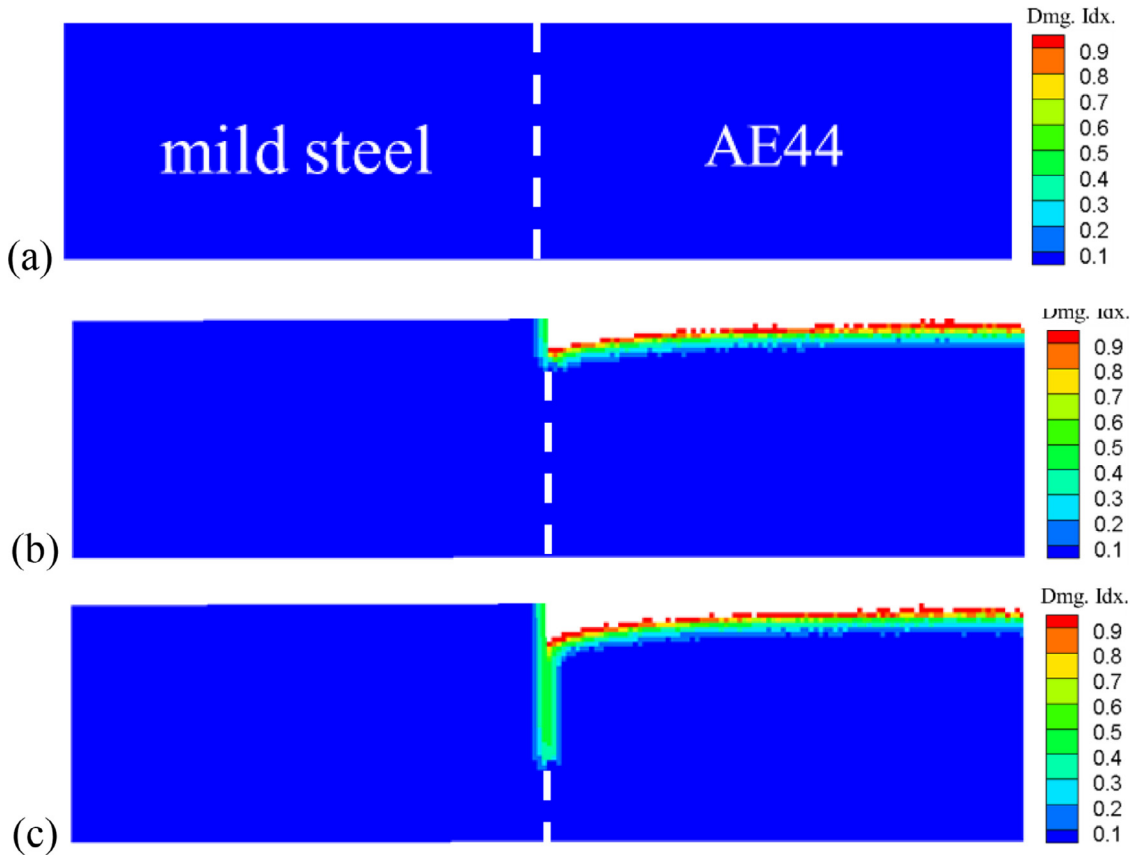

Fig. 17. Damage index for the AE44 – mild steel galvanic couple under stress corrosion cracking at (a) $t = 0$ hrs, (b) $t =$ 36 hrs, and (c) $t =$ 41.6 hrs. See also the movie in Supplementary Materials.

putational cost by creating new nodes and increasing the bandwidth of matrices. The PD model, on the other hand, simplifies this process and allows treatment of complex problems with little effort. For realistic, complex problems, the advantages of PD formulations over traditional methods stand out.

6. Conclusion

A new peridynamic (PD) model for coupled galvanic corrosion and fracture was introduced. The coupled model consists of a PD electrostatic solver to compute the electric potential distribution over the electrolyte domain, a reformulated PD corrosion dissolution model which is applicable to problems with highly non-uniform current densities along arbitrary-shape corroding surfaces (a common occurrence in galvanic corrosion problems), and a linear elastic-brittle fracture PD model.

The reformulated PD corrosion dissolution model was established based on the electrochemical view of the corrosion process. This change enabled an analytical calibration for the corrosion rate and replaced the original integro-differential equation for corrosion dissolution with an ordinary differential equation, leading to a simplified algorithm/implementation and decreased computational cost of simulation compared to the original PD corrosion model. The new model works well even in cases where the current density is highly location-dependent, or when the curvature of the corrosion surface is high (near reentrant corners, for example), as in the case of galvanic corrosion.

The model was verified for a 2D uniform corrosion case in terms of the initial electric potential and current density, and time-dependent corrosion depth. Validating the model against experimental results available from the literature for two galvanic couples (AE44 (Mg alloy) – mild steel and AE44 – AA6063 (Al alloy)) was performed. Results obtained with an FEM-based model built using COMSOL were compared with the PD results. It was found that for FEM-based or phase-field models of corrosion in galvanic couples, a “step-down” needs to be artificially inserted in the geometry at the material interface of the couple in order for these models to produce reasonable results. The step appears to be necessary in models based on partial differential equations because of difficulties in assigning proper boundary conditions at the galvanic couple interface, to correctly initialize the motion of the corrosion front. The need for introducing such geometrical artifacts in a model reduces its generality. Moreover, such artificial modifications to the sample geometry may lead to erroneous results when mechanical loadings are applied to a galvanic couple system, because the stress profile near the interface would be different from the actual one, at least in the early stages of the corrosion process. If there is a strong stress-dependency of the corrosion rate, the likelihood of obtaining wrong results for coupled problems (e.g., galvanic corrosion and fracture) may be further enhanced. The PD model introduced here does not require the artificial change in geometry at the interface to obtain results that match the experimental observations.

A coupled corrosion-fracture problem was solved using the new PD model, demonstrating how fracture can initiate and grow from the sharp trench created by galvanic corrosion. This showed the model’s potential for simulating failure caused by the combined galvanic corrosion attack and mechanical loadings.

Declaration of Competing Interest

The authors declare that they have no known competing financial interests or personal relationships that could have appeared to influence the work reported in this paper.

Credit authorship contribution statement

Jiangming Zhao: Methodology, Software, Writing – original draft, Writing – review & editing, Validation. **Siavash Jafarzadeh:** Methodology, Software, Writing – review & editing. **Mohammad Rahmani:** Software, Investigation, Visualization. **Ziguang Chen:** Methodology, Writing – review & editing. **Yong-Rak Kim:** Methodology, Supervision. **Florin Bobaru:** Conceptualization, Methodology, Writing – review & editing, Supervision, Project administration, Funding acquisition.

Acknowledgments

This work has been supported in part by the US National Science Foundation CMMI CDS&E Grant No. 1953346 (program manager Joanne Culbertson) and by a Nebraska System Science award. This work was completed utilizing the Holland Computing Center of the University of Nebraska, which receives support from the Nebraska Research Initiative.

Supplementary materials

Supplementary material associated with this article can be found, in the online version, at doi:10.1016/j.electacta.2021.138968.

Appendix A. Imposing boundary conditions in PD elastic and electrostatic solvers

Unlike classical local methods, the BCs in peridynamic models are intrinsically nonlocal. However, when solving practical problems, imposing local-type BCs in nonlocal/PD models is usually desired/needed because, in reality, conditions (on the unknown function values or its flux) are imposed at the surfaces of a body, not through a finite layer near the surface. The natural representation of such conditions (based on measurements) is via local BCs. Various methods to impose local BCs in PD models have been investigated in [32,56,57].

For the elastic solver in this work, the local BCs involved (see the example in Section 5) is of the Dirichlet type, and the accuracy of the BCs is not a major concern considering the purpose of the example. Therefore, we assign the value of the Dirichlet BCs directly to those PD nodes nearby, as described in Section 5.

The electrostatic solver, however, involves Robin-type BCs and requires more accurate representation of the local BCs to be enforced. Therefore, we use the fictitious nodes method (FNM) [32,57,58]. In FNM for PD models, certain constraints are specified on the fictitious region $\widetilde{\Omega} = \{\boldsymbol{x} \notin \Omega | \text{distance}(\boldsymbol{x},\ \partial\Omega) < \delta\}$ (the "collar" outside of the solution domain Ω shown in Fig. A1), so that desired local BCs on $\partial\Omega$ are satisfied or approximately satisfied. There are a couple of different FNMs to enforce local BCs in PD models. In this paper, we use the autonomous mirror-based one (or mirror FNM) [16], which is designed to handle arbitrary boundary shapes, to enforce the local BCs at metal surfaces for the electrostatic solver. The fictitious region overlaps a solid region with thickness δ below the metal surface, as shown in Fig. A2. A brief review of the autonomous mirror FNM and a simplification performed for the problem in this work are provided next .

Consider a body occupying the domain $\Omega \in \mathbb{R}^d$, $d = 2$ or 3, and an extended fictitious region $\widetilde{\Omega} = \{\boldsymbol{x} \in \mathbb{R}^d \setminus \Omega | \text{distance}(\boldsymbol{x},\ \partial\Omega) < \delta\}$, as shown in Fig. A3. The mirror FNM assigns the constraint $\tilde{u}(\boldsymbol{x})$ at each $\boldsymbol{x} \in \tilde{\Omega}$ based on $u(\boldsymbol{x}^R)$ and $u(\boldsymbol{x}^P)$ in which $\boldsymbol{x}^P = \text{OProj}_{\partial\Omega}(\boldsymbol{x})$ is the orthogonal projection of $\boldsymbol{x}$ onto $\partial\Omega$ and $\boldsymbol{x}^R = \text{Ref}_{\partial\Omega}(\boldsymbol{x}) = \boldsymbol{x} + 2(\boldsymbol{x}^P - \boldsymbol{x})$ is the reflection, or mirror point, of $\boldsymbol{x}$ through/across $\partial\Omega$. For $\boldsymbol{x} \in \tilde{\Omega}$, when $\partial\Omega_{\boldsymbol{x}} = \{\partial\Omega \cap H_{\boldsymbol{x}}\}$ is continuous and the normal to $\partial\Omega_{\boldsymbol{x}}$ at each $\boldsymbol{y} \in \partial\Omega_{\boldsymbol{x}}$ is unique (i.e., $\partial\Omega_{\boldsymbol{x}} \in G^1$), we have

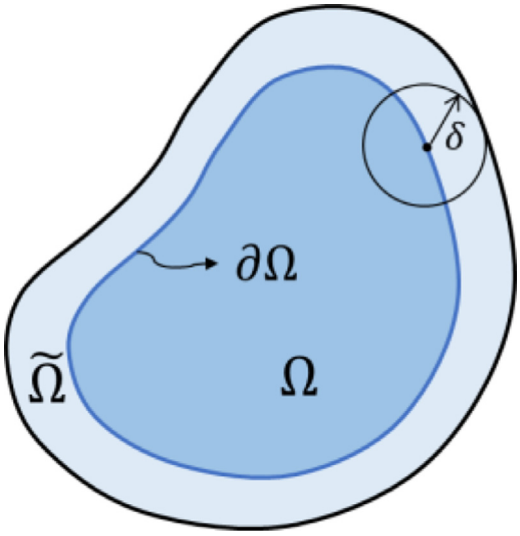

Fig. A1. Schematic of a PD domain (Ω), its boundary ($\partial\Omega$), and its fictitious region ($\tilde{\Omega}$).

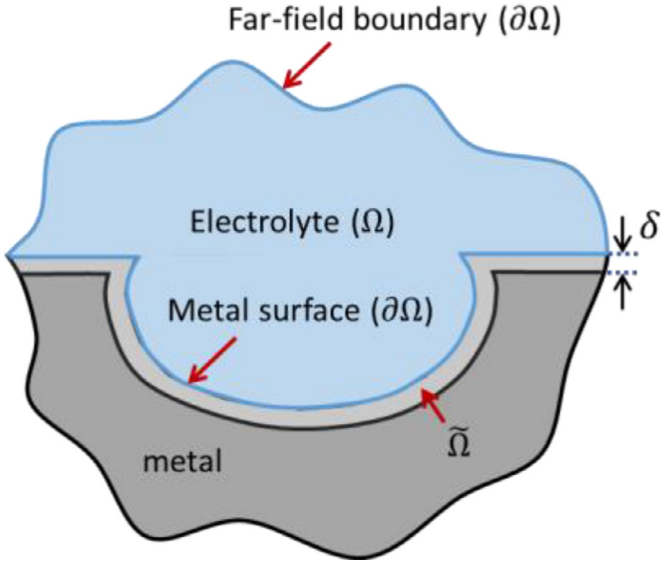

Fig. A2. An illustration of the electrolyte domain (Ω), boundaries ($\partial\Omega$) and fictitious region ($\tilde{\Omega}$) in the PD electrostatic model for a general corrosion problem. The PD horizon size is δ.

$\overrightarrow{\boldsymbol{x}\boldsymbol{x}^P} = \alpha\boldsymbol{n}(\boldsymbol{x}^P)$, in which $\alpha \in \mathbb{R}^-$ and $\boldsymbol{n}(\boldsymbol{x}^P)$ is the outward unit normal vector at $\boldsymbol{x}^P$.

In the mirror FNM, to impose the local Dirichlet BC $u(\boldsymbol{x}) = u_{\text{D}}(\boldsymbol{x})$ for $\boldsymbol{x} \in \partial\Omega_{\text{D}}$ and the Neumann BC $\nabla_{\boldsymbol{n}} u(\boldsymbol{x}) = q$ for $\in \partial\Omega_{\text{N}}$, $\tilde{u}(\boldsymbol{x})$ at $\boldsymbol{x} \in \tilde{\Omega}_{\text{D}}$ is assigned as:

$$\tilde{u}(\boldsymbol{x}) = 2u\left(\boldsymbol{x}^P\right) - u\left(\boldsymbol{x}^R\right) \tag{A1}$$

and $\tilde{u}(\boldsymbol{x})$ at $\boldsymbol{x} \in \tilde{\Omega}_{\text{N}}$ is assigned as:

$$\tilde{u}(\boldsymbol{x}) = u\left(\boldsymbol{x}^R\right) + \|\boldsymbol{x} - \boldsymbol{x}^R\| q \tag{A2}$$

respectively. For the local Robin BC $\nabla_{\boldsymbol{n}} u(\boldsymbol{x}) = f(u(\boldsymbol{x}))$ for $\in \partial\Omega_{\text{R}}$, we have, for $\boldsymbol{x} \in \tilde{\Omega}_{\text{R}}$:

$$\tilde{u}(\boldsymbol{x}) = u\left(\boldsymbol{x}^R\right) + \|\boldsymbol{x} - \boldsymbol{x}^R\| f\left(u\left(\boldsymbol{x}^P\right)\right) = u\left(\boldsymbol{x}^R\right) + \|\boldsymbol{x} - \boldsymbol{x}^R\| f\left(\frac{u\left(\boldsymbol{x}^R\right) + \tilde{u}(\boldsymbol{x})}{2}\right) \tag{A3}$$

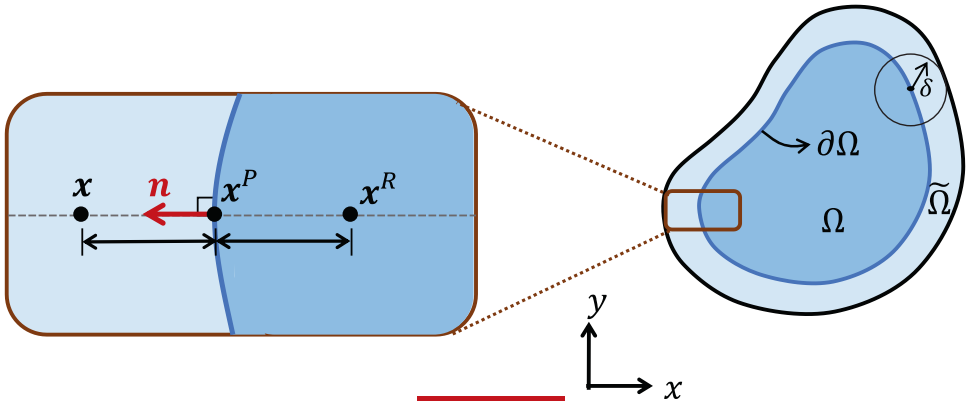

Fig. A3. A schematic of orthogonal projection $\boldsymbol{x}^P$ of $\boldsymbol{x}$ onto $\partial\Omega$ and the reflection $\boldsymbol{x}^R$of $\boldsymbol{x}$ through/across $\partial\Omega$ in mirror-based FNM [32].

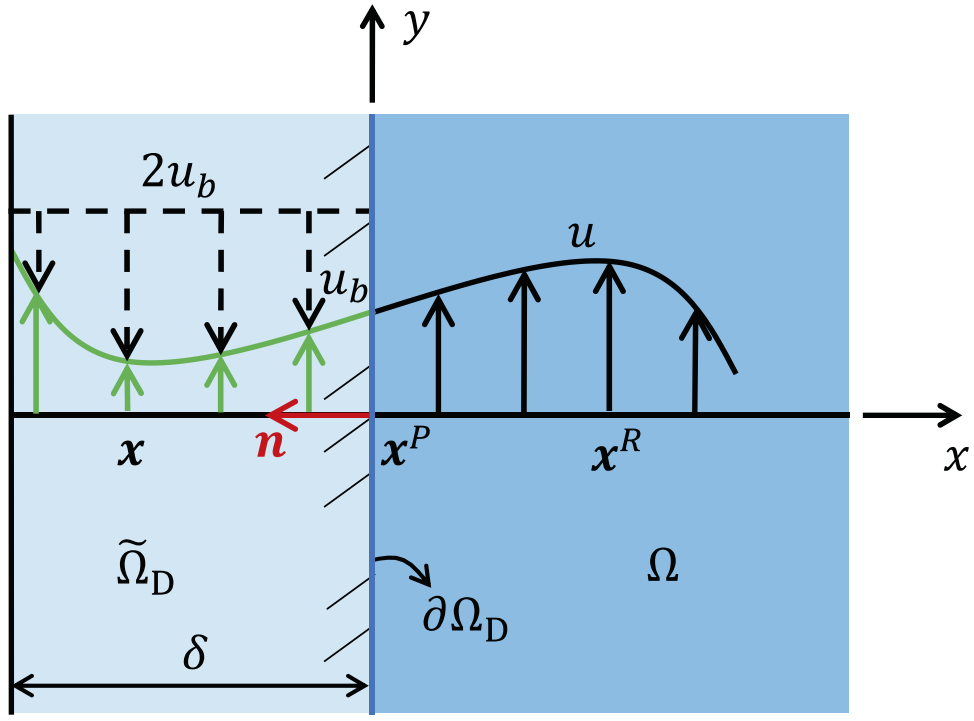

Fig. A4. Illustration of enforcing a local Dirichlet BC in the mirror FNM (redrawn from [32]).

in which the approximation $u(\boldsymbol{x}^P) = \frac{u(\boldsymbol{x}^R)+\tilde{u}(\boldsymbol{x})}{2}$ is made by assuming that the value of u, or $\tilde{u}$, between $\boldsymbol{x}$ and $\boldsymbol{x}^R$ are close to a linear distribution. $\tilde{u}(\boldsymbol{x})$ in Eq. (A3) requires to be solved using a nonlinear solver if function f is nonlinear. Constraints applied on fictitious nodes vary with the solution step. See Fig. A4 for illustrations of how local Dirichlet BCs are enforced in the mirror FNM at each solution step.

For the nonlinear robin boundary condition (at the electrode surfaces) in the galvanic corrosion problem we are solving (see Section 4.2), instead of using a nonlinear solver to solve Eq. (A3), one can replace Eq. (A3) by:

$$\tilde{\phi}(\boldsymbol{x}) = \phi\left(\boldsymbol{x}^R\right) - \frac{W(w_0)}{b} \tag{A4}$$

for $\boldsymbol{x} \in \tilde{\Omega}_R$ where $y = W(w_0)$ is the Lambert W function which satisfies $ye^y = w_0$ and

$$w_0 = -\frac{i_0 \ln 10}{2\sigma\beta} \times \|\overrightarrow{\boldsymbol{x}\boldsymbol{x}^R}\| \times 10^{\left(\frac{\frac{\phi\left(\boldsymbol{x}^R\right)+\tilde{\phi}(\boldsymbol{x})}{2}-\phi_0}{\beta}\right)} \tag{A5}$$

where i_0, σ, β and ϕ_0 are parameters determined by the polarization curve and given in Table 3.

Appendix B. Computing effective corrosion depth

The corrosion depth distribution for a problem with general geometry is usually measured, when available, in the direction normal to the original surface. For the problems considered in this work, that direction is the vertical direction. Therefore, we will measure the depth at each horizontal coordinate x. For a fair comparison of corrosion depth obtained by our PD model and by a classical model (analytical or numerical) or experiments, we will consider both the fully corroded region ($(d(\boldsymbol{x}, t) = 1)$ and the diffusion-based corrosion layer ($d(\boldsymbol{x}, t) \in (0, 1)$) when computing the total mass loss. The effective corrosion depth can then be computed at $x = x_0$ as:

$$z_h(x_0, t) = \frac{1}{C_{\text{solid}} - C_{\text{sat}}} \int_{\psi(x_0,t)} [C_{\text{solid}} - C(x_0, y, t)]dy \tag{B1}$$

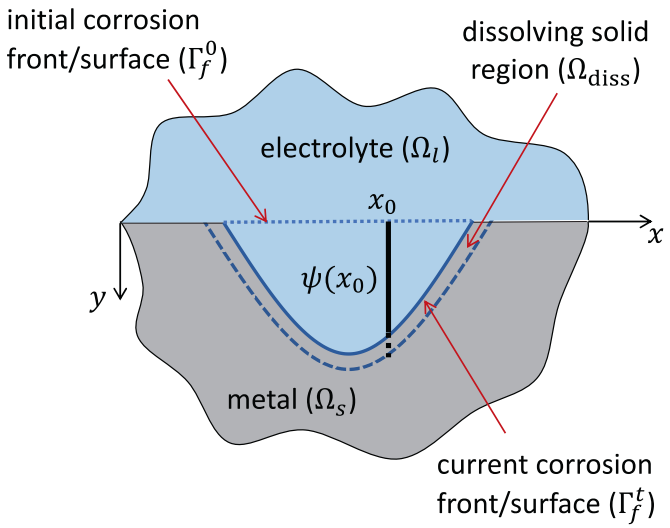

Fig. B1. A schematic of $\psi(x_0)$ over which the PD effective corrosion depth is computed in this work.

where $\psi(x_0, t) = \{\boldsymbol{x}(x, y)|x = x_0$ and $d(\boldsymbol{x}, t = 0) = 0$ and $d(\boldsymbol{x}, t) > 0\}$. The nodes with $d(\boldsymbol{x}, t = 0) = 0$ are those solid at the initial time, while nodes with $d(\boldsymbol{x}, t) > 0$ include liquid and partially damaged ones at the current time. The schematic of $\psi(x_0)$ is shown in Fig. B1.

Appendix C. COMSOL modeling of galvanic corrosion

In COMSOL MultiPhysics®, the dissolution/corrosion process is modeled through the deformation of the boundary using the Arbitrary Lagrangian-Eulerian Method [47]. The deformation is determined by relating the boundary velocity to the electrode corrosion velocity, by the following equation:

$$V_{\text{diss, tot}} = \frac{\partial \boldsymbol{y}}{\partial t} \cdot \boldsymbol{n}|_{\text{anode}} = \sum_j \frac{M_j}{\rho_j} \sum_k \frac{\vartheta_{j,k}\, i_k}{q_k\, F} \tag{C1}$$

where $\boldsymbol{n}$ is the normal vector to the boundary, M_j and ρ_j are molar mass and density of the species j, respectively, $\vartheta_{j,k}$, i_k and q_k are the stoichiometric coefficient of species j, local current density, and the number of participating electrons, respectively, associated with the electrode reactions of index k.

While Eq. (C1) assumes that deformation/dissolution occurs only in the normal direction of the dissolving electrode (anode) boundary, a pointwise constraint is applied to non-dissolving boundaries (cathode) to prevent any dissolution in their normal directions (zero normal displacement):

$$\mathrm{d}\boldsymbol{y} \cdot \boldsymbol{n}|_{\text{cathode}} = 0. \tag{C2}$$

Such treatments may cause challenges for cases with shared nodes at the anode-cathode interface (e.g., the galvanic corrosion shown in Fig. 11 (a)), where the deformation/dissolution may grow into the cathode. To resolve this issue, one may extend the cathode boundary by introducing a small geometric step at the cathode-anode interface, as shown in Fig. C1.

To build the geometry with small step incorporated at the anode-cathode interface the whole domain was constructed using two separate shapes with a difference in height. The two shapes were then connected using the *Booleans and Partitions* module. For the physics of the problem, the *secondary current distribution* and *deformed geometry* modules were used. Then, the electrolyte domain and two electrode surfaces were defined in the model. The cathodic reduction reaction was assigned to the cathode electrode surface, while the anodic corrosion reaction and the resulting boundary movement were defined at the anode electrode surface. The stoichiometric coefficients for dissolving-depositing species were defined for the anode part. To apply a constraint for the planar non-depositing walls in order to enforce a zero boundary movement in the normal direction of surfaces other than the anode, zero normal displacement BC was used in the Multiphysics setting.

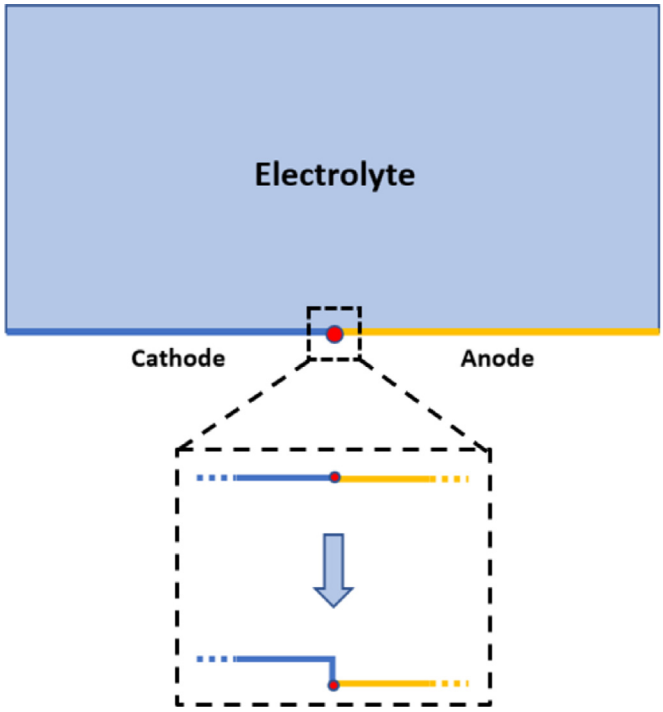

Fig. C1. A schematic of the artificial geometric step at the interface between the anode and the cathode.

Table C1.
Convergence study on the maximum corrosion depth as the height of the initial step decreases, for the AE44 – AA6063 galvanic couple.

Step height (mm)	No. of elements	Max. corrosion depth (mm)
1	1001	0.236905914
0.5	1040	0.240754949
0.2	1078	0.249791228
0.1	1180	0.255897817
0.01	1886	0.259696086
0.001	3850	0.260926697
0.0001	8464	0.261126347

For the COMSOL modeling of the galvanic corrosion problem in Fig. 11 (a), the FE mesh at the initial stage is shown in Fig. C2. There are in total 7 one-node vertex elements, 183 two-node edge elements and 7189 three-node triangular elements, while the number of mesh points is 3687. As we explained above, the small step-down (0.1mm) at the interface between the anode and the cathode is necessary.

The height of this vertical geometric step controls the mesh resolution. Table C1 represents the result for maximum corrosion depth as the height of the step decreases, for the AE44 – AA6063 galvanic couple.

Appendix D. Galvanic corrosion of a AE44 – AA6063 couple

In this appendix, we use the AE44 – AA6063 galvanic couple test the PD and COMSOL models and compare their results with the experimental data provided in [3]. The coefficients used to fit

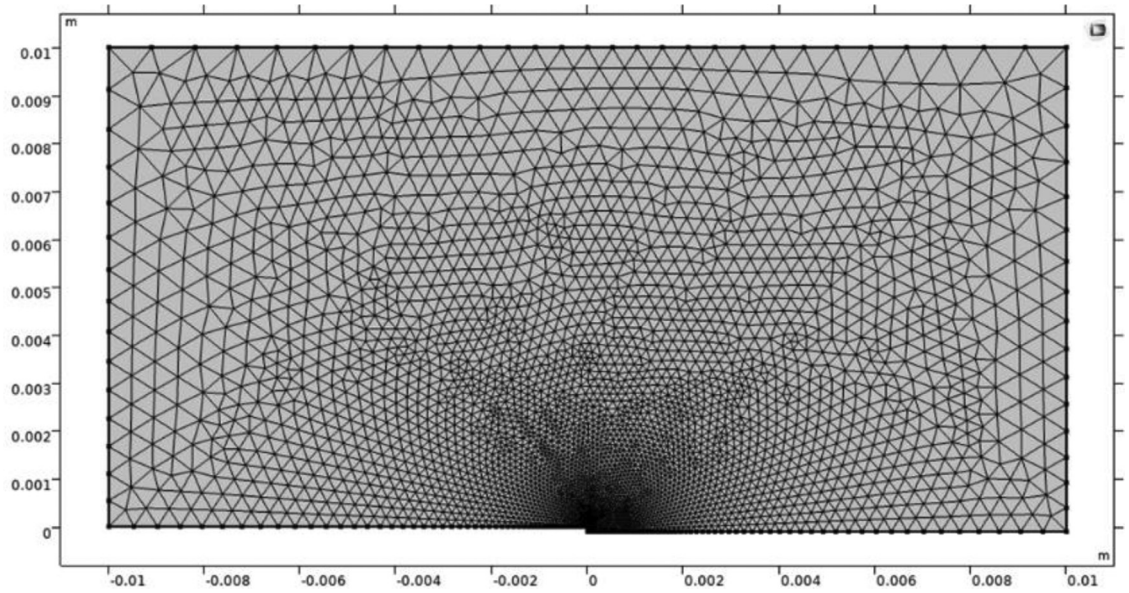

Fig. C2. Finite element mesh in COMSOL for the galvanic cell shown in Fig. 11 (a). Notice the artifical step on the bottom side.

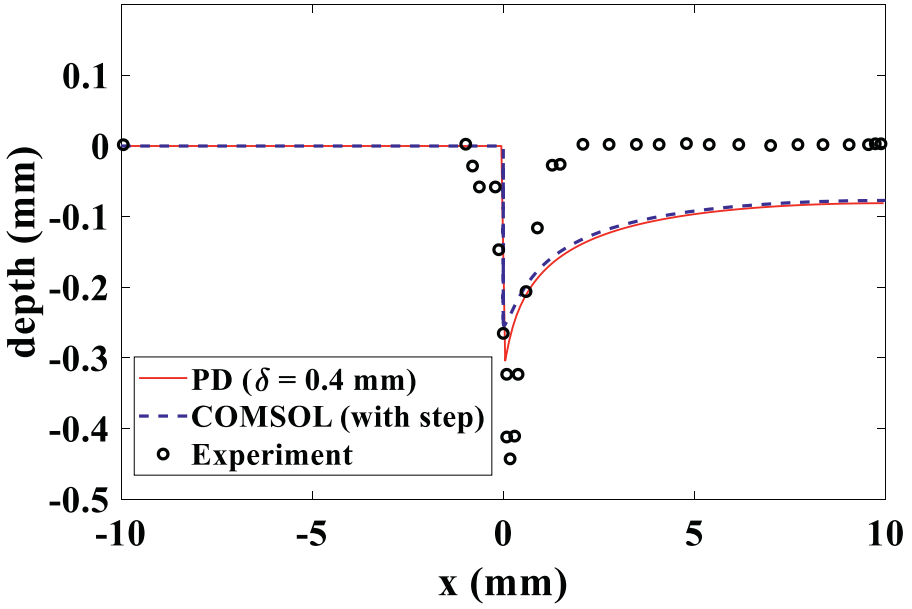

Fig. D1. Quantitative comparison of the final corrosion depth for AE44 – AA6063 galvanic couple between experimental measurement [3], PD simulation and COMSOL simulation.

Table D1.
Data used in the Tafel's equation for AA6063 [2].

	i_0 (A/m^2)	b_c (V)	φ_0 (V, SCE)
AA6063 $\phi \leq -1.363$	0.142	−0.0701	−1.363
$\phi > -1.363$	0.142	−0.0051	−1.363

the polarization curve for AA6063 are shown in Table D1, while those for AE44 can be found in Table 3.

The quantitative comparison of the final corrosion depth between experimental measurement, PD simulation and COMSOL simulation (with the artificial step at the joint included), after 3 days of corrosion, is shown in Fig. D1. As we can see, the corrosion depth obtained from PD simulation agrees with that from the COMSOL simulation. However, they have two significant differences compared with the corrosion depth from the experiment. First, in the experiment, the corrosion does not take place exactly along the interface between two materials. Some part of the AA6063 (which is supposed to be cathode) is also corroded. Second, in the experiment, the corrosion trench is localized near the interface, and is very deep, while the computations show a much shallower trench and considerable reach of corrosion along the AE44 surface. It is highly possible that some other forms of corrosion, such as crevice and micro-galvanic corrosions, take place at the interface and play a significant role here. While we did not consider these mechanisms into our model here, some of them have been separately investigated with PD formulations (see [35,55]), and future developments will include them.

References

[1] S. Jafarzadeh, Z. Chen, F. Bobaru, Computational modeling of pitting corrosion, Corros. Rev. 37 (2019) 419–439, doi:10.1515/corrrev-2019-0049.

[2] K.B. Deshpande, Validated numerical modeling of galvanic corrosion for couples: magnesium alloy (AE44)–mild steel and AE44–aluminium alloy (AA6063) in brine solution, Corros. Sci. 52 (2010) 3514–3522, doi:10.1016/j.corsci.2010.06.031.

[3] K.B. Deshpande, Experimental investigation of galvanic corrosion: comparison between SVET and immersion techniques, Corros. Sci. 52 (2010) 2819–2826, doi:10.1016/j.corsci.2010.04.023.

[4] I. Adlakha, B.G. Bazehhour, N.C. Muthegowda, K.N. Solanki, Effect of mechanical loading on the galvanic corrosion behavior of a magnesium-steel structural joint, Corros. Sci. 133 (2018) 300–309, doi:10.1016/j.corsci.2018.01.038.

[5] Imanian A., Amiri M., Phase field modeling of galvanic corrosion, arXiv preprint (2018). http://arxiv.org/abs/1804.08517.

[6] W. Mai, S. Soghrati, New phase field model for simulating galvanic and pitting corrosion processes, Electrochim. Acta 260 (2018) 290–304, doi:10.1016/j.electacta.2017.12.086.

[7] W. Sun, G. Liu, L. Wang, T. Wu, Y. Liu, An arbitrary Lagrangian–Eulerian model for studying the influences of corrosion product deposition on bimetallic corrosion, J. Solid State Electrochem. 17 (2013) 829–840, doi:10.1007/s10008-012-1935-9.

[8] K. Wang, C. Li, Y. Li, J. Lu, Y. Wang, X. Luo, Multi-physics analysis of the galvanic corrosion of Mg-steel couple under the influence of time-dependent anisotropic deposition film, J. Magnes. Alloy (2021), doi:10.1016/j.jma.2020.11.022.

[9] Z. Chen, F. Bobaru, Peridynamic modeling of pitting corrosion damage, J. Mech. Phys. Solids 78 (2015) 352–381, doi:10.1016/j.jmps.2015.02.015.

[10] S. Jafarzadeh, Z. Chen, J. Zhao, F. Bobaru, Pitting, lacy covers, and pit merger in stainless steel: 3D peridynamic models, Corros. Sci. 150 (2019) 17–31, doi:10.1016/j.corsci.2019.01.006.

[11] Z. Chen, S. Jafarzadeh, J. Zhao, F. Bobaru, A coupled mechano-chemical peridynamic model for pit-to-crack transition in stress-corrosion cracking, J. Mech. Phys. Solids 146 (2021) 104203, doi:10.1016/j.jmps.2020.104203.

[12] R. Duddu, N. Kota, S.M. Qidwai, An extended finite element method based approach for modeling crevice and pitting corrosion, J. Appl. Mech. 83 (2016) 081003, doi:10.1115/1.4033379.

[13] S. Jafarzadeh, Z. Chen, F. Bobaru, Peridynamic modeling of repassivation in pitting corrosion of stainless steel, Corrosion 74 (2018) 393–414, doi:10.5006/2615.

[14] E. McCafferty, Introduction to Corrosion Science, Springer, NY, 2010 New York, New York, doi:10.1007/978-1-4419-0455-3.

[15] C. Lin, H. Ruan, S.Q. Shi, Phase field study of mechanico-electrochemical corrosion, Electrochim. Acta 310 (2019) 240–255, doi:10.1016/j.electacta.2019.04.076.

[16] J. Zhao, S. Jafarzadeh, Z. Chen, F. Bobaru, An algorithm for imposing local boundary conditions in peridynamic models on arbitrary domains, engrXiv (2020), doi:10.31224/osf.io/7z8qr.

[17] D.A. Jones, Principles and Prevention of Corrosion, Macmillan, 1992.

[18] A.J. Bard, L. Fulkner, Electrochemical Methods, Fundamental Applications, John Wiley & Sons, Inc., 2001.

[19] S.M. Sharland, C.P. Jackson, A.J. Diver, A finite-element model of the propagation of corrosion crevices and pits, Corros. Sci. 29 (1989) 1149–1166, doi:10.1016/0010-938X(89)90051-6.

[20] C. Tsuyuki, A. Yamanaka, Y. Ogimoto, Phase-field modeling for pH-dependent general and pitting corrosion of iron, Sci. Rep. 8 (2018) 12777, doi:10.1038/s41598-018-31145-7.

[21] S.A. Silling, Reformulation of elasticity theory for discontinuities and long-range forces, J. Mech. Phys. Solids 48 (2000) 175–209, doi:10.1016/S0022-5096(99)00029-0.

[22] S.A. Silling, E. Askari, A meshfree method based on the peridynamic model of solid mechanics, Comput. Struct. 83 (2005) 1526–1535, doi:10.1016/j.compstruc.2004.11.026.

[23] E. Madenci, E. Oterkus, Peridynamic Theory and Its Applications, Springer, NY, 2014 New York, New York, doi:10.1007/978-1-4614-8465-3.

[24] F. Bobaru, G. Zhang, Why do cracks branch? A peridynamic investigation of dynamic brittle fracture, Int. J. Fract. 196 (2015) 59–98, doi:10.1007/s10704-015-0056-8.

[25] F. Bobaru, J.T. Foster, P.H. Geubelle, S.A. Silling, Handbook of Peridynamic Modeling, CRC press, 2016, doi:10.1201/9781315373331.

[26] S.A. Silling, R.B. Lehoucq, Peridynamic theory of solid mechanics, Adv. Appl. Mech. (2010) 73–168, doi:10.1016/S0065-2156(10)44002-8.

[27] Y.D. Ha, F. Bobaru, Studies of dynamic crack propagation and crack branching with peridynamics, Int. J. Fract. 162 (2010) 229–244, doi:10.1007/s10704-010-9442-4.

[28] J.T. Foster, S.A. Silling, W.W. Chen, Viscoplasticity using peridynamics, Int. J. Numer. Methods Eng. 81 (2010) 1242–1258, doi:10.1002/nme.2725.

[29] Y.L. Hu, N.V. De Carvalho, E. Madenci, Peridynamic modeling of delamination growth in composite laminates, Compos. Struct. 132 (2015) 610–620, doi:10.1016/j.compstruct.2015.05.079.

[30] F. Bobaru, M. Duangpanya, The peridynamic formulation for transient heat conduction, Int. J. Heat Mass Transf. 53 (2010) 4047–4059, doi:10.1016/j.ijheatmasstransfer.2010.05.024.

[31] F. Bobaru, M. Duangpanya, A peridynamic formulation for transient heat conduction in bodies with evolving discontinuities, J. Comput. Phys. 231 (2012) 2764–2785, doi:10.1016/j.jcp.2011.12.017.

[32] S. Oterkus, E. Madenci, A. Agwai, Peridynamic thermal diffusion, J. Comput. Phys. 265 (2014) 71–96, doi:10.1016/j.jcp.2014.01.027.

[33] J. Zhao, Z. Chen, J. Mehrmashhadi, F. Bobaru, Construction of a peridynamic model for transient advection-diffusion problems, Int. J. Heat Mass Transf. 126 (2018) 1253–1266, doi:10.1016/j.ijheatmasstransfer.2018.06.075.

[34] Z. Chen, G. Zhang, F. Bobaru, The influence of passive film damage on pitting corrosion, J. Electrochem. Soc. 163 (2016) C19–C24, doi:10.1149/2.0521602jes.

[35] S. Jafarzadeh, Z. Chen, F. Bobaru, Peridynamic modeling of intergranular corrosion damage, J. Electrochem. Soc. 165 (2018) C362–C374, doi:10.1149/2.0821807jes.

[36] S. Jafarzadeh, Z. Chen, S. Li, F. Bobaru, A peridynamic mechano-chemical damage model for stress-assisted corrosion, Electrochim. Acta 323 (2019) 134795, doi:10.1016/j.electacta.2019.134795.

[37] Z. Chen, D. Bakenhus, F. Bobaru, A constructive peridynamic kernel for elasticity, Comput. Methods Appl. Mech. Eng. 311 (2016) 356–373, doi:10.1016/j.cma.2016.08.012.

[38] S. Li, Z. Chen, F. Wang, B. Cui, L. Tan, F. Bobaru, Analysis of corrosion-induced diffusion layer in ZK60A magnesium alloy, J. Electrochem. Soc. 163 (2016) C784–C790, doi:10.1149/2.1001613jes.

[39] S. Li, Z. Chen, L. Tan, F. Bobaru, Corrosion-induced embrittlement in ZK60A Mg alloy, Mater. Sci. Eng. A 713 (2018) 7–17, doi:10.1016/j.msea.2017.12.053.

[40] R. Vallabhaneni, T.J. Stannard, C.S. Kaira, N. Chawla, 3D X-ray microtomography and mechanical characterization of corrosion-induced damage in 7075 aluminium (Al) alloys, Corros. Sci. 139 (2018) 97–113, doi:10.1016/j.corsci.2018.04.046.

[41] D. Yavas, P. Mishra, A. Alshehri, P. Shrotriya, K.R. Hebert, A.F. Bastawros, Nanoindentation study of corrosion-induced grain boundary degradation in a pipeline steel, Electrochem. Commun. 88 (2018) 88–92, doi:10.1016/j.elecom.2018.02.001.

[42] J.T. Burns, S. Kim, R.P. Gangloff, Effect of corrosion severity on fatigue evolution in Al–Zn–Mg–Cu, Corros. Sci. 52 (2010) 498–508, doi:10.1016/j.corsci.2009.10.006.

[43] J.R. Shewchuk, An introduction to the conjugate gradient method without the agonizing pain, Tech. Rep. C. Carnegie Mellon Univ. (1994), https://www.cs.cmu.edu/~quake-papers/painless-conjugate-gradient.pdf.

[44] Z. Xu, G. Zhang, Z. Chen, F. Bobaru, Elastic vortices and thermally-driven cracks in brittle materials with peridynamics, Int. J. Fract. 209 (2018) 203–222, doi:10.1007/s10704-017-0256-5.

[45] S. Jafarzadeh, A. Larios, F. Bobaru, Efficient solutions for nonlocal diffusion problems via boundary-adapted spectral methods, J. Peridyn. Nonlocal Model. 2 (2020) 85–110, doi:10.1007/s42102-019-00026-6.

[46] S. Jafarzadeh, L. Wang, A. Larios, F. Bobaru, A fast convolution-based method for peridynamic transient diffusion in arbitrary domains, Comput. Methods Appl. Mech. Eng. 375 (2021) 113633, doi:10.1016/j.cma.2020.113633.

[47] COMSOL, corrosion module user's guide, 2018. https://doc.comsol.com/5.4/doc/com.comsol.help.corr/CorrosionModuleUsersGuide.pdf.

[48] H. Tada, P.C. Paris, G.R. Irwin, The Stress Analysis of Cracks Handbook, 3rd ed., ASME Press, 2000, doi:10.1115/1.801535.

[49] T.L. Anderson, Fracture Mechanics, CRC Press, 2017, doi:10.1201/9781315370293.

[50] A. Katiyar, J.T. Foster, H. Ouchi, M.M. Sharma, A peridynamic formulation of pressure driven convective fluid transport in porous media, J. Comput. Phys. 261 (2014) 209–229, doi:10.1016/j.jcp.2013.12.039.

[51] J.B. Yan, J.Y.R. Liew, M.H. Zhang, J.Y. Wang, Mechanical properties of normal strength mild steel and high strength steel S690 in low temperature relevant to Arctic environment, Mater. Des. 61 (2014) 150–159, doi:10.1016/j.matdes.2014.04.057.

[52] M.M. Avedesian, H. Baker, ASM Specialty Handbook: Magnesium and Magnesium Alloys, ASM International, 1999.

[53] K. Prasad, M. Srinivas, S.V. Kamat, Influence of mixed mode I/III loading on dynamic fracture toughness of mild steel at room and low temperatures, Mater. Sci. Eng. A 590 (2014) 54–59, doi:10.1016/j.msea.2013.09.099.

[54] N. Winzer, A. Atrens, G. Song, E. Ghali, W. Dietzel, K.U. Kainer, N. Hort, C. Blawert, A critical review of the stress corrosion cracking (SCC) of magnesium alloys, Adv. Eng. Mater. 7 (2005) 659–693, doi:10.1002/adem.200500071.

[55] S. Jafarzadeh, J. Zhao, M. Shakouri, F. Bobaru, A peridynamic model for crevice corrosion damage, engrXiv (2021), doi:10.31224/osf.io/fc7xd.

[56] Q. Du, M. Gunzburger, R.B. Lehoucq, K. Zhou, A nonlocal vector calculus, nonlocal volume-constrained problems, and nonlocal balance laws, Math. Model. Methods Appl. Sci. 23 (2013) 493–540, doi:10.1142/S0218202512500546.

[57] Y. Tao, X. Tian, Q. Du, Nonlocal diffusion and peridynamic models with Neumann type constraints and their numerical approximations, Appl. Math. Comput. 305 (2017) 282–298, doi:10.1016/j.amc.2017.01.061.

[58] Q.V. Le, F. Bobaru, Surface corrections for peridynamic models in elasticity and fracture, Comput. Mech. 61 (2018) 499–518, doi:10.1007/s00466-017-1469-1.